Check for updates

View Article Online
View Journal

Dalton Transactions

An international journal of inorganic chemistry

Accepted Manuscript

This article can be cited before page numbers have been issued, to do this please use: P. Kumar, P. Singh, S. Saren, S. Pakira, S. Sri and A. K. Patra, *Dalton Trans.*, 2021, DOI: 10.1039/D1DT00246E.

Volume 46
Number 10
14 March 2017
Pages 3073-3412

Dalton Transactions

An international journal of inorganic chemistry

rsc.li/dalton

ISSN 0306-0012

ROYAL SOCIETY OF CHEMISTRY

COMMUNICATION
Douglas W. Stephen *et al.*
N-Heterocyclic carbene stabilized parent sulfenyl, selenenyl, and tellurenyl cations (XH+, X = S, Se, Te)

This is an Accepted Manuscript, which has been through the Royal Society of Chemistry peer review process and has been accepted for publication.

Accepted Manuscripts are published online shortly after acceptance, before technical editing, formatting and proof reading. Using this free service, authors can make their results available to the community, in citable form, before we publish the edited article. We will replace this Accepted Manuscript with the edited and formatted Advance Article as soon as it is available.

You can find more information about Accepted Manuscripts in the Information for Authors.

Please note that technical editing may introduce minor changes to the text and/or graphics, which may alter content. The journal's standard Terms & Conditions and the Ethical guidelines still apply. In no event shall the Royal Society of Chemistry be held responsible for any errors or omissions in this Accepted Manuscript or any consequences arising from the use of any information it contains.

ROYAL SOCIETY OF CHEMISTRY

rsc.li/dalton

View Article Online
DOI: 10.1039/D1DT00246E

Kinetically Labile Ruthenium(II) Complexes of Terpyridines and Saccharin: Effect of Substituents on Photoactivity, Solvation Kinetics, and Photocytotoxicity

Priyaranjan Kumar[a], Prerana Singh[bc], Sanjoy Saren[a], Sandip Pakira[a], Sri Sivakumar[b], Ashis K. Patra*[a]

Author address: [a]Department of Chemistry, Indian Institute of Technology Kanpur, Kanpur 208016, Uttar Pradesh, India. E-mail: akpatra@iitk.ac.in

[b]Department of Chemical Engineering, DST Thematic Unit of Excellence on Soft Nanofabrication, Indian Institute of Technology Kanpur, Kanpur 208016, Uttar Pradesh, India.

[c]Department of Biological Sciences & Bioengineering, Indian Institute of Technology Kanpur, Uttar Pradesh 208016, India

View Article Online
DOI: 10.1039/D1DT00246E

Abstract

Herein, we designed six kinetically labile ruthenium(II) complexes containing saccharin (sac) and 4′-substituted-2,2:6,2-terpyridines (R-tpy), *viz. trans*-[Ru(sac)$_2$(H$_2$O)$_3$(dmso-*S*)] (**1**) and [Ru^{II}(R-tpy)(sac)$_2$(X)] [X = solvent molecule] (**2−6**). We intentionally kept the labile hydrolysable Ru-X bonds that were potentially activated *via* solvent-exchange reactions. This strategy generates the coordinative vacancy that allows further binding with potential biological targets. To gain insight of the electronic effects of ancillary ligands on Ru-X ligand-exchange kinetics or photoreactions, we have used a series of substituted terpyridines (R-tpy) and studied their solvation kinetics. The ternary complexes were also aimed for their potential utility in the Ru-assisted photoactivated chemotherapy (PACT) synergized with release of saccharin as a highly selective carbonic anhydrase IX (CA-IX) inhibitor, over-expressed in hypoxic tumors. The ternary complexes exhibit distorted octahedral geometry around Ru(II) from two monodentate *transoidal* saccharin in axial position, and tridentate terpyridines and labile solvent molecule at basal plane (**2−6**). We studied their speciation, solvation kinetics, and photoreactivity in the presence of green LED light (λ_{irr} = 530 nm). All the complexes are relatively labile and undergo solvation in coordinating solvents (e.g. DMSO/DMF). The complexes undergo ligand-substitution reaction, their speciation and kinetics were studied by UV-Vis, ESI-MS, ^{1}H-NMR, and structural analysis. We also attempted to access the effect of various substituents on ancillary terpyridine ligand (R-tpy) in photo-reactivity and ligand-exchange reactions. The photo-induced absorption and emission measurements suggested dissociation of the saccharin from Ru-center supporting PACT pathways. Complexes display a significant binding affinity with CT-DNA (K_b ~10^4−10^6 M^{-1}) and bovine serum albumin (BSA) (K_{BSA} ~ 10^5 M^{-1}). The cytotoxicity studied in the dark and the presence of low energy UV-A light (365 nm) in cervical cancer cells (HeLa) and breast cancer cells (MCF7). Photoirradiation of the complexes induces the generation of reactive oxygen species (ROS) accessed using 1,3-diphenylisobenzofuran (DPBF) and intracellular DCFDA assays. The complexes are sufficiently internalized in cancer cells throughout the cytoplasm and nucleus and induce apoptosis studied by staining with dual dyes using confocal microscopy.

View Article Online
DOI: 10.1039/D1DT00246E

Introduction

Ruthenium complexes offer several desirable opportunities to the synthetic inorganic chemist for designing targeted chemotherapeutics. Ruthenium has the flexibility to form covalent bonds with various hard and soft donors (O, N, P, S and halogens, arenes) and wide structural diversity for pharmacological targets. Therefore, the scope and flexibility for structural modulation and peripheral ligand modification are far greater than the platinum drugs. Moreover, ruthenium is more apt for multimodal therapeutic approaches due to its remarkable catalytic activity, redox modulation *via* physiologically accessible oxidation-states (Ru^{II}, Ru^{III}), tunable ligand-exchange kinetics, and excellent photochemistry among d-block elements [1−6]. These multifaceted characters make Ru-complexes at the forefront of medicinal inorganic chemistry for the last two decades [7−11]. The medicinal inorganic chemists can satisfy their keen intuition, and creative designs for studying multi-targeted metallodrugs due to the immense opportunity and diversity Ru-complexes offers in multiple directions. Ruthenium complexes can exhibit their anticancer activity *via* activation of a wide range of cellular pathways, offering to reinforce many cell-death mechanisms. Such a strategy gives the prospect to tackle acquired drug resistance by Pt-drugs and their harmful side effects [12−15]. Ru-compounds' biological targets include DNA, proteins, enzymes, genes, and lipids having a significant role in tumor growth, survival, and metabolism [16]. The high uptake of Ru-complexes to cancerous tissue and lowered systematic toxicities are often correlated with its advantageous periodic similarity with iron. The iron-transporter protein transferrin (Tf) meets the high demand of Fe to cancer cells for their faster proliferation and metabolism. The Ru-agents exploit Tf to facilitate their cellular internalization and exhibit tumor selectivity and high dose tolerance compared to the platinum drugs [3].

The inorganic photosensitizers in combination with light and oxygen provide significant opportunities for newer chemotherapeutic modalities-photodynamic therapy (PDT) or photoactivated chemotherapy. The electronically excited states of certain metal complexes possess easily accessible long-lived triplet excited states triggered by visible light activation. These excited states undergo a series of photochemical reactions before deactivation to ground states, e.g., photorelease of bioactive ligands, energy transfer to $^3O_2$, redox reactions, etc. [17]. The Ru-photochemistry has been extensively utilized for developing non-invasive and clinically approved PDT agents for cancer which provide selectivity *via* spatiotemporal control [18]. The PDT modality is a strategy of generating cytotoxic reactive oxygen species (ROS) in situ from the photosensitizers

View Article Online
DOI: 10.1039/D1DT00246E

upon excitation of preferably low energy light in the presence of $^3O_2$. Even with the low energy photo-illumination in visible to near-infrared (NIR) can generate excited-state of the metal complexes, which can either transfer electrons to $^3O_2$ to form superoxide (O_2^-), peroxide (O_2^{2-}), and hydroxyl radicals ($^\bullet$OH) (Type 1) or transfer energy to generate $^1O_2$ (Type II) as major cytotoxic species [19–21]. Ru-polypyridyl complexes are a suitable choice as photosensitizers over the organic chromophores because of superior absorption in the phototherapeutic window, low-lying excited triplet states, and facile electron or energy transfer reactions to the biological substrates. Moreover, the luminescent Ru(II) complexes are apt for cellular imaging probes, understanding mechanism of actions, and theranostic applications [22]. Recently, McFarland and coworkers reported the first Ru(II)-based PDT agent, TLD1433 containing α-terthienyl conjugated imidazo[4,5-*f*][1,10]-phenanthroline photosensitizer and two 4,4′-dimethyl-2,2′ bipyridine ligands. TLD1433 has entered phase 1b human clinical trials to treat non-muscle-invasive bladder cancer (NMIBC) and showed promising results [23, 24]. The solely O_2-dependence is a major limitation of PDT modality, limiting its applicability for the treatment of solid and aggressive tumors considering their hypoxic nature. Therefore, the treatment of solid hypoxic tumors remains challenging for both classical chemotherapy and PDT. The combination of light to Ru-photocaged complexes can activate them to dissociative ^{3}MLCT triplet excited electronic states, which interconvert further to ^{3}MC electronic states. These processes end up forming new cytotoxic chemical entities, known as photoactivated chemotherapy (PACT), providing spatiotemporal control of the treatment modality. Interestingly, Ru-complexes with PACT applications do not primarily require oxygen and have the potential to generate vacant sites on Ru by cleavage and photosubstitution of usually monodentate or bidentate ligands selectively. Both the activated metal center and/or photo-substituted ligand can impart biological activity in synergy [25–29]. The metal-solvated photoproduct can express binding and damage to the targets such as DNA like platins [29]. Therefore, the PACT strategy can be elegantly utilized for targeting solid hypoxic tumors. S. Bonnet and coworkers recently reported nicotinamide phosphoribosyltransferase (NAMPT) inhibitor-containing red-light-activated (λ_{ex} = 625 nm) Ru-caged complex namely [Ru(tpy)(biq)(L)]$^{2+}$ (biq = 2,2′-biquinoline, tpy = 2,2′;6′-2′′-terpyridine and L = 4-[({[4-(2-methyl-2-propanyl)phenyl]sulfonyl}amino)methyl]-N-(3-pyridinyl)benzamide) capable of triggering the cytotoxic ligand in oxygen-independent manner for skin and lung cancers [30]. Hypoxia is a major obstacle in chemotherapy and photochemotherapy resulting in poor prognosis and drug resistance.

View Article Online
DOI: 10.1039/D1DT00246E

To date, efficient hypoxia targeting agents are very limited in the literature. Thus, developing such complexes is worthwhile to treat clinically challenging tumors with characteristics of poor prognosis and resistance to multimodal chemotherapy and phototherapy [31−33].

In the context of exploiting various cancer hallmarks, the altered metabolic pathways of cancer cells (Warburg effect) produce a considerably high amount of lactic acid, making tumour microenvironment acidic [34]. Despite this adverse condition, cancer cells survive by local upregulation of pH mediated from overexpressed carbonic anhydrase (CA)-IX and XII. Saccharin (ortho-sulfobenzimide) is a potential inhibitor for CA-IX in nanomolar affinity, having more than 1000-fold selectivity over the rest of the CA-isoforms. The inhibitory action of saccharin (sac) may negatively affect tumor cells' survival by lowering intracellular pH [35−37]. Therefore, the saccharin releasing complexes could be a potential strategy to target hypoxic tumors [38].

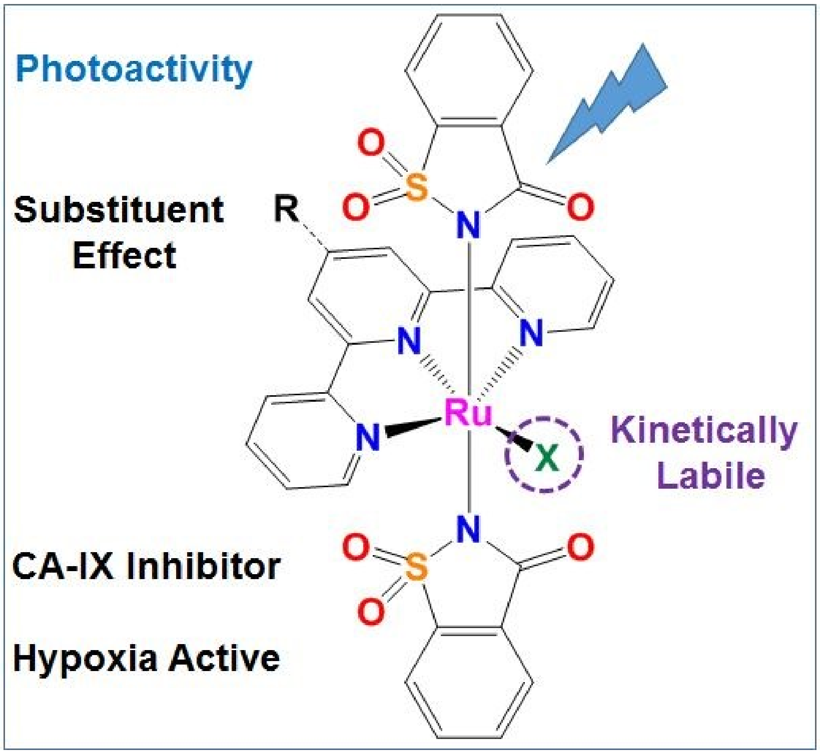

Scheme 1. The rationale for design of [Ru^{II}(R-tpy)(sac)$_2$(X)] (**2-6**) complexes with substituted 4′-{(2-pyrrolyl (**2**)/furyl (**3**)/thienyl (**4**)/pyridyl (**5**) and 3-pyridyl (**6**)}-2,2′:6,2-terpyridines (R-tpy) and X = solvents (CH$_3$CN, dmso, and H$_2$O) studied in this work.

Here, we have thoughtfully designed six Ru(II) complexes of bioactive saccharin (sac) ligands and 4′-substituted terpyridines (R-tpy) (**2**−**6**) with the intended labile exchangeable solvent coordination

View Article Online
DOI: 10.1039/D1DT00246E

site to form activated Ru(II) complexes. These activated complexes are expected to interact with biological targets such as nucleobases, oligonucleotides, amino acids, DNA, or proteins during their intracellular passage (Scheme 1). Therefore, it is important to understand the equilibrium kinetics of the formation of various ligand-exchange species and their fate in physiological conditions. To gain insight into the electronic effects of peripheral ligands on photoreactions' kinetics or ligand-exchange kinetics, we have used a series of substituted terpyridine (R-tpy). Moreover, R-tpy also acts as effective photosensitizers and DNA-binder with varying 4′-substituents for modulation of photophysical and electronic properties. The choice of prognostic biomarker sac was based on its potentials to inhibit carbonic anhydrase-IX (CA-IX) in possible synergism with photoactivated chemotherapy (PACT) of Ru-polypyridyl complexes. Recently, we have reported the photo-induced saccharin dissociation and DNA damage activity of octahedral Ru(II) complexes of saccharin containing dipyridoqunoxaline (dpq) and dipyridophenazine (dppz) following ROS generation and PACT pathways [39].

We report here the synthesis, spectral characterizations, solid-state structures, solution chemistry and photoreactivity, and binding studies with DNA and serum proteins of a series of ternary [Ru^{II}(R-tpy)(sac)$_2$(X)] (**2**-**6**) complexes containing accessible labile site (Ru-X) for feasible bioreactivity. The complexes undergo solvent-exchange reactions in H_2O, DMF, CH_3CN, and DMSO, demonstrating their kinetic lability. Interestingly, the complexes showed unique photo-induced responses upon exposure of low energy green LED light (λ_{irr} = 530 nm), corresponding to photoactivation and probable release of saccharin. The cytotoxicity and photocytotoxicity of complexes **1**, **2,** and **4** were evaluated from MTT assay in HeLa and MCF7 cancer cell lines. Formation of reactive oxygen species (ROS) upon photoirradiation was studied from the degradation of 1,3-diphenylisobenzofuran (DPBF) and staining of cancer cells with ROS-sensitve 2',7'-dichlorodihydrofluorescein diacetate (H_2DCFDA) dye. The emissive complexes displayed significant permeability, uptake, and induce apoptosis as determined by acridine orange/ethidium bromide (AO/EB) dual staining. The complexes are envisioned as potential ROS-mediated photoactivated chemotherapeutic agents.

DOI: 10.1039/D1DT00246E

Results and Discussion

Synthesis, Characterization and Physiochemical aspects

All the Ru(II) complexes were synthesized in good yield from *cis*-[Ru(dmso-*S*)$_3$(dmso-*O*)Cl$_2$], sodium saccharinate dihydrate (Na$^+$sac$^-$•2H$_2$O) and 4′-substituted-2,2′:6′,2″-terpyridines (R-tpy) at ambient conditions (Scheme 2). The reaction of Na$^+$Sac with a warm solution of *cis*-[Ru(dmso-*S*)$_3$(dmso-*O*)Cl$_2$] in methanol resulted in the formation of *trans*-[Ru(sac)$_2$(H$_2$O)$_3$(dmso-*S*)] (**1**). The series of ternary complexes [Ru^{II}(R-tpy)(sac)$_2$(X)] (**2**−**6**) were synthesized from the binary complex **1** upon reaction with 4′-{(2-pyrrolyl (**2**)/furyl (**3**)/thienyl (**4**)/pyridyl (**5**) and 3-pyridyl (**6**)}-terpyridines (R-tpy). All the complexes were isolated as crystalline solids after work-up and remain stable in ambient conditions. The complexes were characterized by ESI-MS, UV-Vis, FT-IR, NMR, electrochemical analysis, fluorescence, and molecular structure was confirmed by single-crystal X-ray diffraction studies. The selected results obtained from these physicochemical measurements are shown in Table 1. The ESI-MS(+) analyses showed the presence of molecular ion peaks (M$^+$) corresponding to the complexes with the expected isotopic distribution pattern of Ru (Figs. S1−S6). The structural identity and purity of the complexes in solution were further evaluated from ^{1}H NMR (Figs. S7−S12). Noticeably, a slight deshielded peak corresponding to DMSO-*d*$_6$ in addition to referenced solvent (DMSO-*d*$_6$) was observed, which originated from the coordination to the labile site present in the complexes. All the complexes display characteristic chemical shift (δ ppm) values corresponding to substituted R-tpy and sac in the aromatic region of the ^{1}H-NMR spectrum. Both ESI-MS and NMR analyses suggest the structural integrity of ternary speciation in solution as determined in solid-state. The FT-IR of complexes **1**−**6** showed the strong carbonyl ($\nu_{C=O}$) stretching frequencies (sac) ranging 1630−1643 cm^{-1} (Fig. S13). The strong symmetric (ν_{sym}) and asymmetric (ν_{asym}) stretching frequencies corresponding to the sulphonyl (ν_{SO_2}) group of sac ligand vary within 1146−1157 cm^{-1} and 1286−1292 cm$^{-1,}$ respectively [40]. Complexes **2**−**6** showed a lowered $\nu_{C=O}$ than binary complex **1** with the minimum value for complex **4** ($\nu_{C=O}$ = 1630 cm^{-1}). The ternary complexes **2**−**6** with varying 4′-terpyridine substitution are interesting in their distinct electronic properties. *Trans*-[Ru(sac)$_2$(H$_2$O)$_3$(dmso-*S*)] (**1**) showed two weak absorption bands at 275 nm (ε = 2640 M^{-1}cm^{-1}) and 365 nm (ε = 370 M^{-1}cm^{-1}) in DMF representing the ligand-based $\pi\rightarrow\pi^*$ transition and metal-to-ligand charge transfer (^{1}MLCT) from Ru(dπ) → sac(π^*) [41]. The absorptions in the UV-region (284−350 nm) for the complexes **2**−**6** in DMF arise from the ligand-

DOI: 10.1039/D1DT00246E

centered (^{1}LC) $\pi\rightarrow\pi^*$ transitions (Fig. 1(a) and Table 1). All the complexes displayed an intense absorption band in the visible region of 496−560 nm assignable as ^{1}MLCT originating from spin-allowed Ru(dπ)→tpy(π^*) electronic transition [42, 43]. Interestingly, 4′-(2-pyrrolyl/furyl/thienyl)-R-tpy substitutions of the complexes **2**−**4** showed a red-shift of ~ 8−20 nm in their ^{1}MLCT bands than the 4′-(2-pyridyl/3-pyridyl)-tpy indicating underlying electronic effects of the substituents. The complexes with 2-furyl (**3**) and 2-thienyl (**4**) substituents showed similar MLCT bands (~505 nm) with a higher molar absorptivity of the later complex. The 2-pyrrolyl substituent in complex **2** showed red-shift ~ 10-20 nm compared to the rest of the ternary complexes suggesting a relatively low-energy ^{1}MLCT state. The 3-pyridyl-tpy in **6** leads to an additional MLCT shoulder at 560 nm. The UV-Vis absorption spectra of the complexes **1**−**6** in 1% (v/v) DMF−5 mM Tris-HCl/NaCl buffer (pH = 7.2) showed small blue shifts of both the $\pi\rightarrow\pi^*$ and Ru(dπ)→tpy(π^*) bands compared with DMF solvent (Fig. S14 and Table S1). The complexes display multiple irreversible redox responses in their cyclic voltammograms assignable to $Ru^{II/III}$ and tpy ligands (Fig. 1(b), Fig. S15 and Table 1). The $Ru^{II}\rightarrow Ru^{III}$ potential ranges from 1.01−1.12 V vs. Ag/AgCl, while saccharin remained redox- inactive in these potential ranges [42, 44, 45].

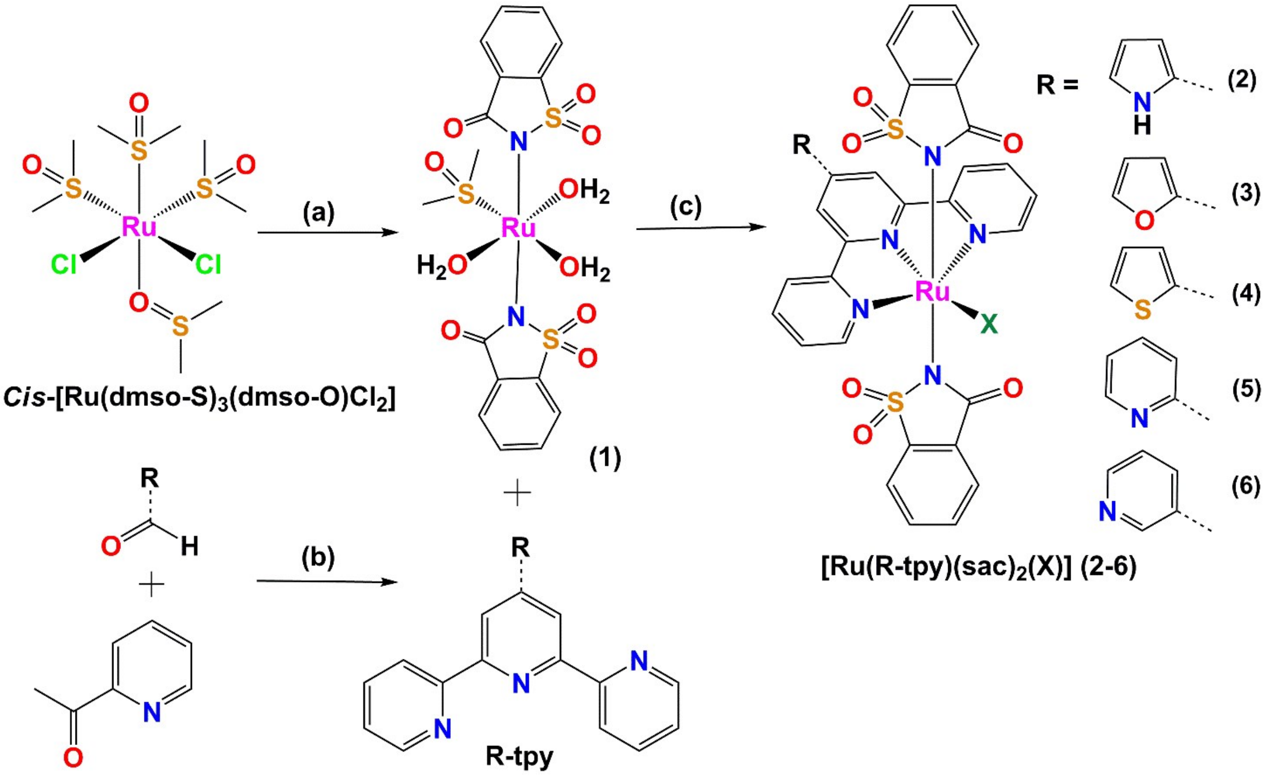

View Article Online
DOI: 10.1039/D1DT00246E

Scheme 2. General route for the synthesis of Ru(II) complexes: *trans*-[Ru(sac)$_2$(H$_2$O)$_3$(dmso-*S*)] (**1**) and [Ru(R-tpy)(sac)$_2$(X)] (X = solvent) (**2−6**). The reaction reagents and conditions: (a) 2 equiv. Na$^+$sac$^-$.2H$_2$O (sac = saccharin), MeOH, 3 h reflux; (b) KOH, NH$_3$(aq), EtOH, overnight stirring; (c) **1** (MeOH), 4′-substituted-2,2′:6′,2″-terpyridine (CHCl$_3$), 12 h reflux.

The lower redox potentials in case complexes **2−6** than **1** indicate the increased electron density at Ru(II)-centre implies that the R-tpy ligands are more likely better σ-donors. The complexes **3** and **4** with 2-furyl and 2-thienyl substituents showed similar Ru^{II}→Ru^{III} potential but the isomeric complexes **6** showed the higher *E* (V) for the couple Ru$^{II/III}$ than complex **5**.

The luminescence spectra of the ligands in DMF showed R-tpy ligands are highly emissive and showed fluorescence ranging 360–395 nm upon excitation at 280 nm (Fig. S16 (b)). The saccharin (sac) was found only weakly emissive at λ_{em} = 440 nm along with a weak shoulder at 345 nm. The complexes **1−6** showed a ligand-centered (^{1}LC) broad emissions ranging 430−460 nm (λ_{ex} = 360 nm), and another emission peak at 407 nm (**2−6**) and 412 nm (**1**) respectively (Fig.1(d), Table 1) [46]. Upon excitation at 280 nm, the complexes show two emission bands in the range of 345–451 nm with λ_{em} ~ 345 nm and ~450 nm respectively (Fig. S17 and Table S1). The resemblance of emission spectral profile of sac and complexes suggested the fluorescence emission of the complexes originating mainly from sac ligands for complexes **1–5** while both the **3-pytpy** and **sac** centered emission was observed for complex **6**. The excitation of MLCT bands of the complexes showed very poor emission, possibly due to closer ^{3}MLCT and metal-centered excited (^{3}MC) states which favor radiationless thermal deactivation (Fig. S18) [47]. Moreover, the presence of labile Ru-X (solv.) bond will facilitate the non-radiative decay of triplet Ru-centered excited states *via* vibrational energy transfer (VET). The excitation spectra of the ligands are shown in Fig. 16 (a). The excitation spectra of complexes at λ_{em} = 450 nm in DMF showed a peak at ~ 285 nm and broad peaks ranging 330−430 nm (Fig. 1(c)).

View Article Online
DOI: 10.1039/D1DT00246E

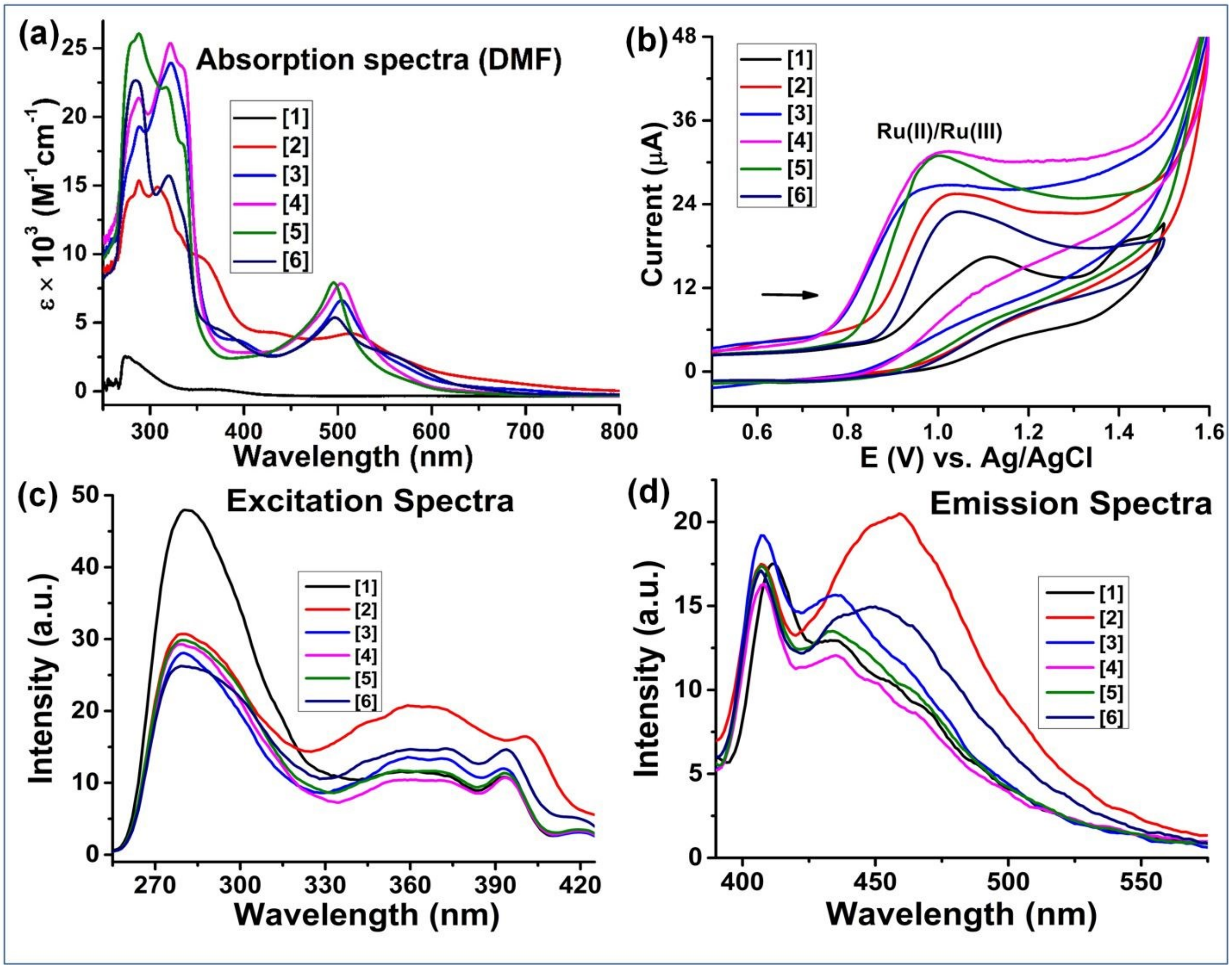

Fig. 1. (a) Absorption spectra of the complexes **1–6** in DMF at 298 K. (b) The cyclovoltametric responses of complexes **1–6** (1 mM) in DMF showing the Ru^{II}/Ru^{III} redox couple [supporting electrolyte: 0.1 M $^{n}Bu_4NClO_4$; working electrode: glassy carbon; counter electrode: Pt-wire, scan rate: 50 mVs^{-1}]. (c) Overlay of the excitation spectra of the complexes **1–6** (10 μM) with λ_{em} = 450 nm. (d) The emission spectra of the complexes **1**–**6** (10 μM) in DMF. [λ_{ex} = 360 nm, ex. slit width = 10 nm, em. slit width = 10 nm, T = 298 K].

Table 1. Selected photophysical and electrochemical data of complexes **1**−**6**.

Complex	$\lambda_{max}{}^{a}$/nm, (ε/ $\times 10^3$ $M^{-1}cm^{-1}$)	$\lambda_{em}{}^{b}$/nm	IR^{c}/cm^{-1} ($\nu_{C=O}$)	(ν_{SO_2}) sym/asym	$E_{pc}{}^{d}(Ru^{II/II})$
`1	275 (2.64), 365 (0.37)	412, 435	1643	1148/1292	1.12
2	288 (18.33), 310 (17.77), 350 (11.86), 515 (5.02)	407, 460	1642	1148/1290	1.05
3	288 (18.81), 322 (24.67), 505 (6.73)	407, 435	1642	1146/1287	1.02
4	288 (20.53), 322 (24.60), 504 (7.59)	407, 435	1630	1157/1296	1.02
5	288 (25.18), 316 (21.39), 496 (7.79)	407, 433	1631	1147/1288	1.01

View Article Online
DOI: 10.1039/D1DT00246E

6	284 (29.56), 320 (20.25), 497 (6.89), 560 (3.32)	407, 450	1636	1148/1286	1.05

[a]UV–visible determined absorption peak maximum and molar extinction coefficient in DMF. [b]Fluorescence emission maxima with λ_{exc} = 360 nm. [c]In KBr pellets. [d]Redox potential (V) for the couple $Ru^{II/III}$ vs. Ag/AgCl in the presence of 0.1 M tetrabutylammonium perchlorate (TBAP) as supporting electrolyte in DMF.

Single crystal X-ray structures

The *trans*-[Ru(sac)$_2$(H$_2$O)$_3$(dmso-*S*)] (**1**) and [Ru(R-tpy)(sac)$_2$(X)] (X = solvent) (**3–5**) were crystallized using slow evaporation under ambient conditions. Our efforts to crystallize complexes **2** and **6** remained unsuccessful. All the complexes crystallized in the triclinic *P*-1 space group with two molecules in the unit cell. The ORTEP views of the molecular structures with labeled heteroatoms are shown in Fig. 2, and the unit cell packing diagrams are shown in Fig. S19 in ESI. The detailed crystallographic parameters are given in Table S2 and the selected bond lengths are shown in Table S3 and S4 in ESI. The crystal structure of *trans*-[Ru^{II}(sac)$_2$(H$_2$O)$_3$(dmso-*S*)] (**1**) showed distorted octahedral geometry coordinating of three H$_2$O, one dmso (*S*-donor) in equatorial plane, and two axial saccharinates as N-donor in *trans*-conformation. The [Ru^{II}(R-tpy)(sac)$_2$(X)] (X = solvent) (**3–5**) showed distorted octahedral {RuN$_5$(solvent)} geometry with three basal sites coordinated to *N*$_3$-donor terpyridine ligands (R-tpy), two axial sites bound to the *N*-donor saccharinate (*trans*). The sixth equatorial site is coordinated to a solvent molecule (X), [X = CH$_3$CN (**3**); H$_2$O (**4**, **5**)]. The Ru-X site is expected to be kinetically labile and can facilitate further ligand-exchange reactions.

View Article Online
DOI: 10.1039/D1DT00246E

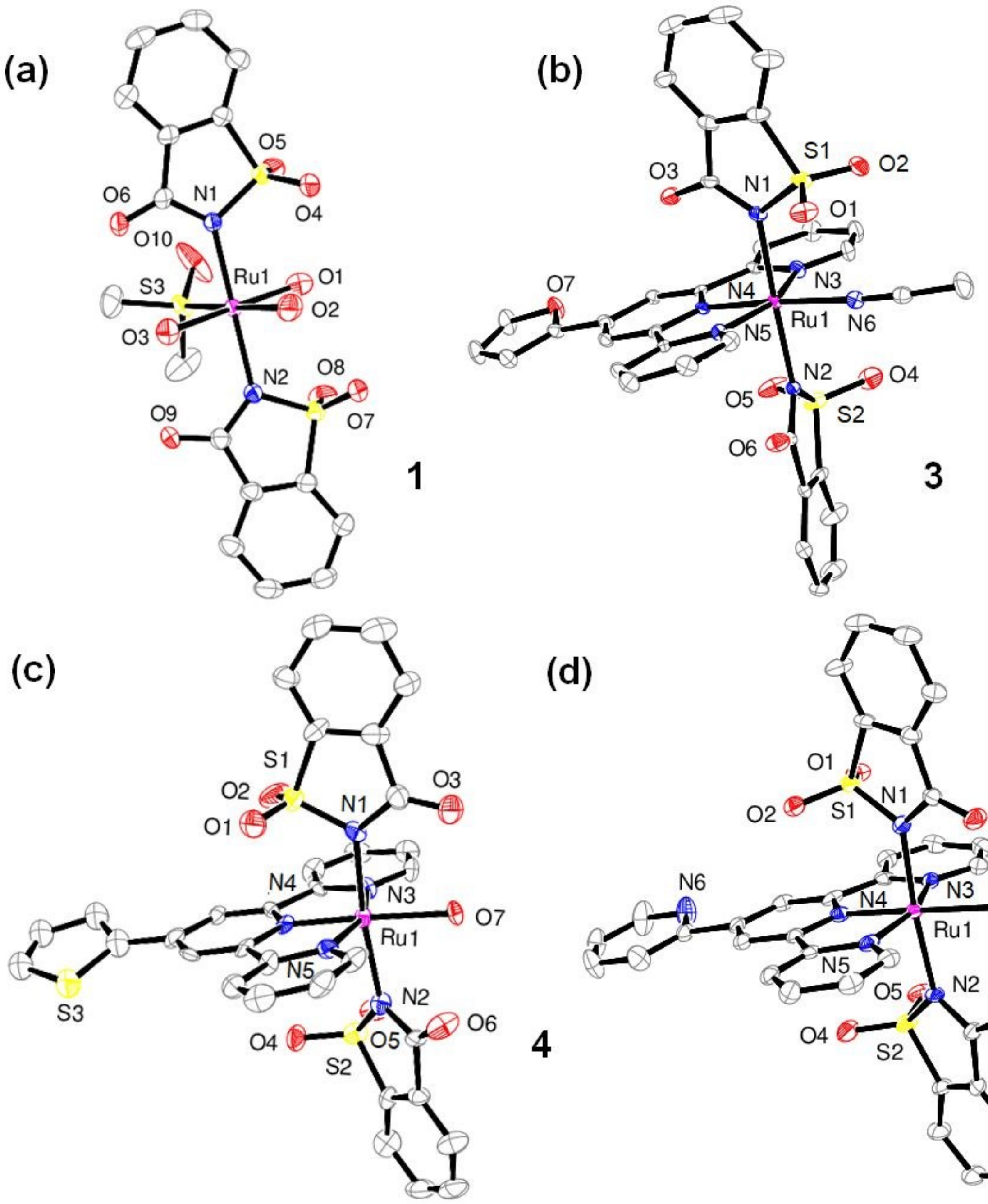

Fig. 2. The ORTEP view of the molecular structure of *trans*-[Ru(sac)$_2$(H$_2$O)$_3$(dmso-*S*)] (**1**) and [Ru(R-tpy)(sac)$_2$(X)] (**1**, **3**, **5)** with labeled heteroatoms. The thermal ellipsoids are drawn at its 50% probability level. The hydrogen atoms were omitted for clarity.

View Article Online
DOI: 10.1039/D1DT00246E

Table 2. Selected Ru(II)-sac/tpy bond lengths and the dihedral angle between the sac ligands

Complex	1	3	4	5
Ru–N$_{(sac)}$^{a} (Å)	2.128(4)	2.124(3)	2.131(8)	2.114(3)
Ru–N4$_{(tpy)}$^{b} (Å)	–	1.944(3)	1.927(7)	1.921(3)
Dihedral angle^c	7.30°	71.55°	40.39°	9.75°

^{a}Smallest bond length for Ru–N$_{sac}$. ^{b}Ru–N bond length *trans* to solvent coordination site. ^{c}The dihedral angle between the [Ru1N1S1C7] and [Ru1N2S2C14] planes containing sac ligands.

The longest and shortest bond lengths in complex **1** are Ru−S(dmso) and Ru−O3(OH$_2$), respectively. A gradual decrease of the average Ru-(N)$_{sac}$ and Ru-N$_{tpy}$ bond lengths were observed in **3**−**5** than complex **1** reveals the substituents' associated electronic effects at 4′-tpy. The Ru-N bond distances in complexes were in the range of reported analogous Ru(II) complexes [39, 48−51]. The shortest Ru-N bonds correspond to the Ru-(N)$_{sac}$ (**1**) and Ru-N4$_{tpy}$ (**3**−**5**) are shown in Table 2, suggesting a better *π*-acceptor ability of pytpy (**5**) than ftpy (**3**) and ttpy (**4**) [52]. The longest bond for complex **3** is Ru−N1(sac) at 2.134(3) Å and for complexes **4** and **5** is Ru1−O7 (OH$_2$) at a distance of 2.191(6) Å and 2.174(2) Å, respectively. Both the saccharinates are a little away from perfectly *trans*-configuration as evidenced from ∠N1-Ru1-N2: 173.27(16)° (**1**), 176.11(13)° (**3**), 172.2(3)° (**4**) 173.30(12)° (**5**). A strong intermolecular long-range *π*−*π* interaction was observed between the saccharin rings at 3.376 Å for **1** and between the R-tpy rings at 3.359 Å (**3**), 3.376 Å (**4**), and 3.356 Å (**5**) and shown in Fig. S20. A significantly higher dihedral angle for complexes **3** (71.55°) and **4** (40.39°) are observed between the saccharin planes compared to complex **1** (7.30°) and **5** (9.75°) (Table 2 and Fig. S21).

Solvation of the Complexes

Ruthenium(II) complexes with a labile site like the Pt(II) drugs show hydrolysis and are believed to be a key step before interacting with the biological targets to exhibit its therapeutic efficacy. The presence of labile Ru-Cl bond(s) is a crucial design criterion as evident from the molecular structures of NAMI-A, KP1019, or half-sandwich Ru-arene complexes (e.g. RAPTA-C) and many recent examples originally inspired form platins. However, the factors that influence Ru-X bond's lability (X = monodentate ligands) or its variation on therapeutic efficacy are not investigated systematically in the literature. Any metallodrug inside the cells obviously encounters a vast array of potential low

View Article Online
DOI: 10.1039/D1DT00246E

or high M.W. biologically relevant species as ligands ranging from H_2O, Cl^-, nucleotides, amino acids, thiols, amino acids, peptides, nucleic acids or proteins, etc. Some of these reactions are desirable for activation of the drug, while rest may lead to significant inactivation, efflux, or create multiple roadblocks to reach the desirable pharmacological targets. Therefore, a sound understanding of the modulation of such reaction kinetics and speciation in the physiological condition is essential. Such pharmacokinetics information is vital in designing a truly effective drug candidate that will survive the complex and competitive cellular environment and able to make its way to the desired site at an effective dose. A deeper understanding of these reactions is also essential to study the mechanism of action of multi-drug resistance (MDR) and how to overcome it. The comparable rates of hydrolysis of Ru(II)-complexes with Pt(II), make them a suitable and alternative choice of metal for Pt(II) in chemotherapy [53]. The rates of solvation/anation reactions can be fine-tuned based on the ancillary ligands' electronic effects and substituents present on it. The ligand substitution kinetics is directly associated with the pharmacokinetic profile of the Ru(II)-drugs; higher ligand-exchange rates usually showcase higher cytotoxicity [54]. The labile Ru(II)-X bonds in [Ru^{II}(R-tpy)(sac)$_2$(X)] (X = solvent) (**2−6**) are expected to undergo a facile hydrolysis to form aqua-complexes followed by anticipated coordination with intracellular biological targets. The solvolysis reaction kinetics of the complexes were studied in DMF and aqueous buffer using UV-vis spectroscopy and in DMSO-d_6 using ^{1}H NMR to understand their lability and *in situ* speciation in solution.

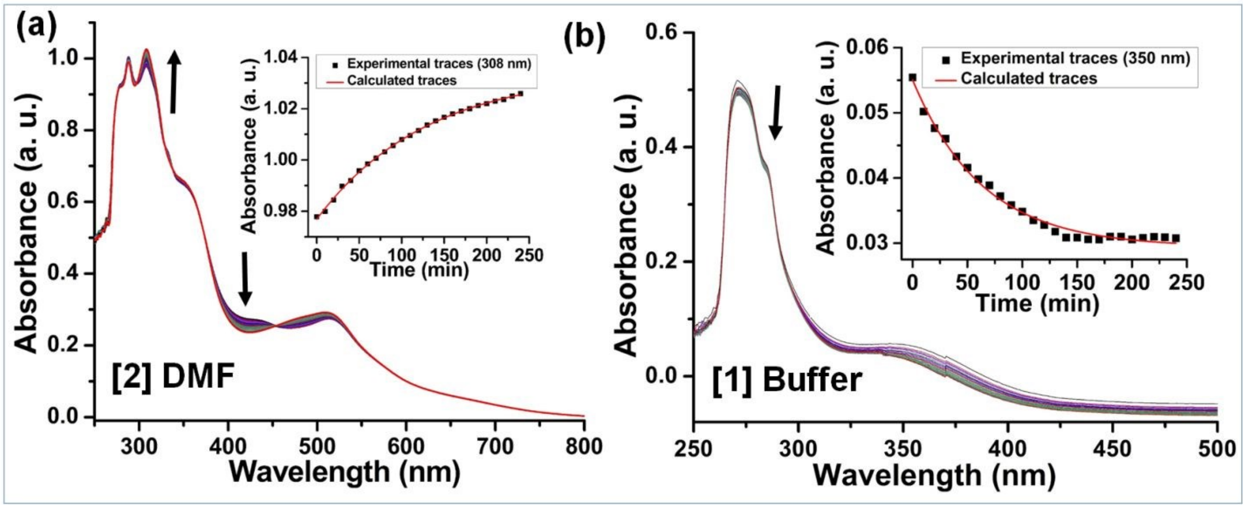

Fig. 3. The electronic absorption changes of the complexes **1** and **2** upon solvation for 240 mins in the dark. (a) The solvation of complex **2** (58 μM) in the presence of DMF. Inset: The pseudo-first-order kinetic fit measured from the changes in $A_{308\ \mathrm{nm}}$ for complex **2** upon solvation with DMF. (b) The hydrolysis kinetics of

View Article Online
DOI: 10.1039/D1DT00246E

complex **1** (222 μM) in the presence of 11% (v/v) DMF−5 mM Tris-HCl/NaCl buffer (pH = 7.2) mixture. Inset: The pseudo first-order kinetic fit of the changes in $A_{350\ \mathrm{nm}}$ upon hydrolysis.

Table 3. The solvation kinetic parameter for the complexes **1**−**6**.

Complex	k^a (s^{-1})	$t_{1/2}{}^b$ (min)	k^c (s^{-1})	$t_{1/2}{}^d$ (min)
1	(8.90±0.90) × 10^{-4}	13.00	(2.6±0.14) × 10^{-4}	44.0
2	(1.30±0.04) × 10^{-4}	90.12	(8.9±1.50) × 10^{-5}	129.78
3	(2.31±0.16) × 10^{-4}	49.93	(5.62±1.80) × 10^{-5}	205.64
4	(2.37±0.10) × 10^{-4}	48.77	(1.99±0.16) × 10^{-4}	58.09
5	(2.44±0.29) × 10^{-4}	47.40	-	-

[a]Solvation rate constant in DMF at 298 K calculated from λ_{abs} = 350 nm (**1**), 308 nm (**2**), 308 nm (**3**), 322 nm (**4**) and 318 nm (**5**). [b]Half –lifetime from first-order kinetics of solvation (DMF). [c]Hydrolysis rate constant at 298 K calculated from λ_{abs} = 350 nm (**1**), 286 nm (**2**), 322 nm (**3**), and 322 nm (**4**). [d]Half –lifetime from first-order kinetics of hydrolysis.

The solvation kinetics of the complexes **1**−**6** were studied in DMF and DMF−5 mM Tris-HCl/NaCl buffer (pH = 7.2) in the dark condition from time-dependent absorption measurement (Fig. 3 and Figs. S22−S24). The UV-Vis spectra of the complexes in DMF or aq. buffer showed

View Article Online
DOI: 10.1039/D1DT00246E

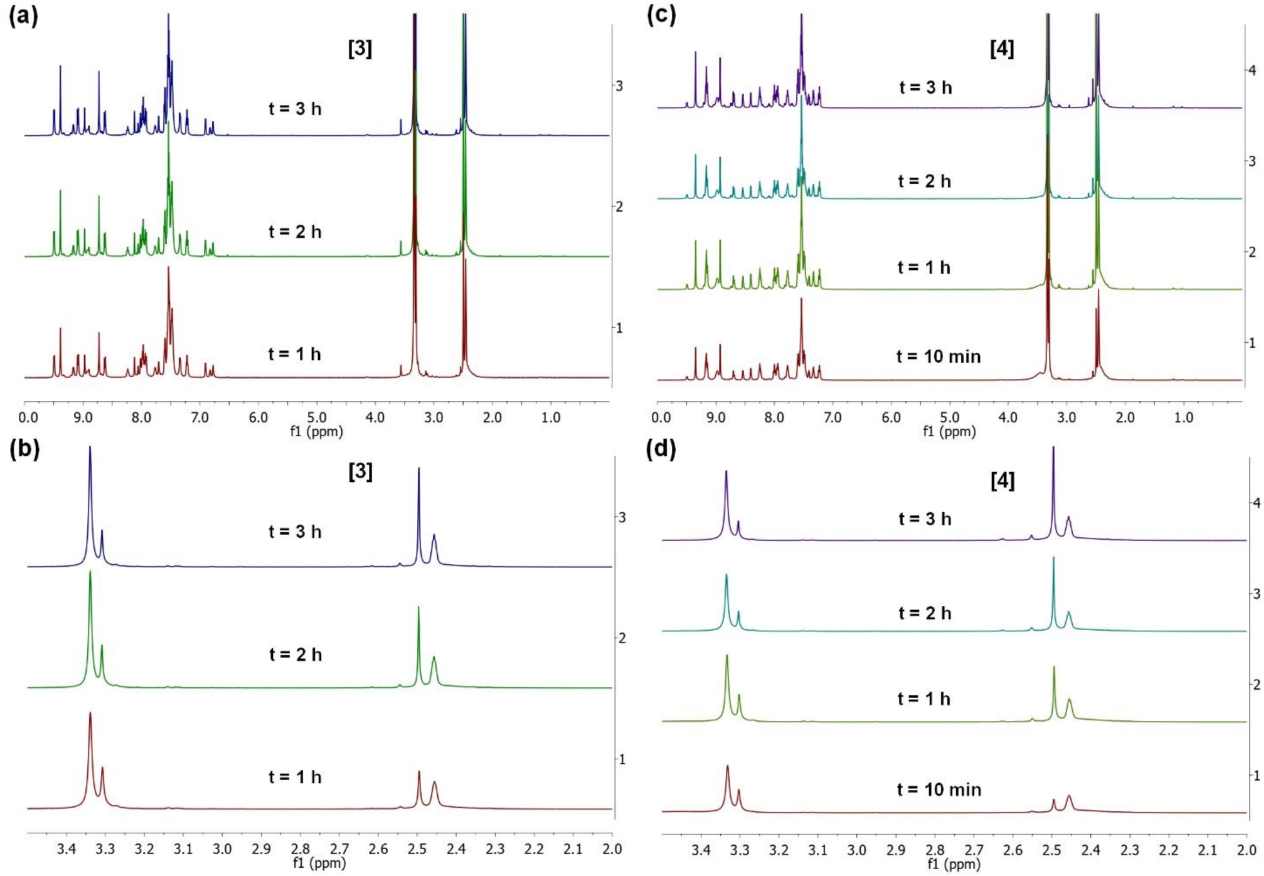

Fig. 4. Time-dependent concomitant evolution of ^{1}H-NMR spectra of the complexes (DMSO-d_6, 500 MHz, 298 K) for 3 h at various ranges: (a, b) [Ru^{II}(furyl-tpy)(sac)$_2$(X)] (**3**), and (c, d) [Ru^{II}(thienyl-tpy)(sac)$_2$(X)] (**4**).

View Article Online
DOI: 10.1039/D1DT00246E

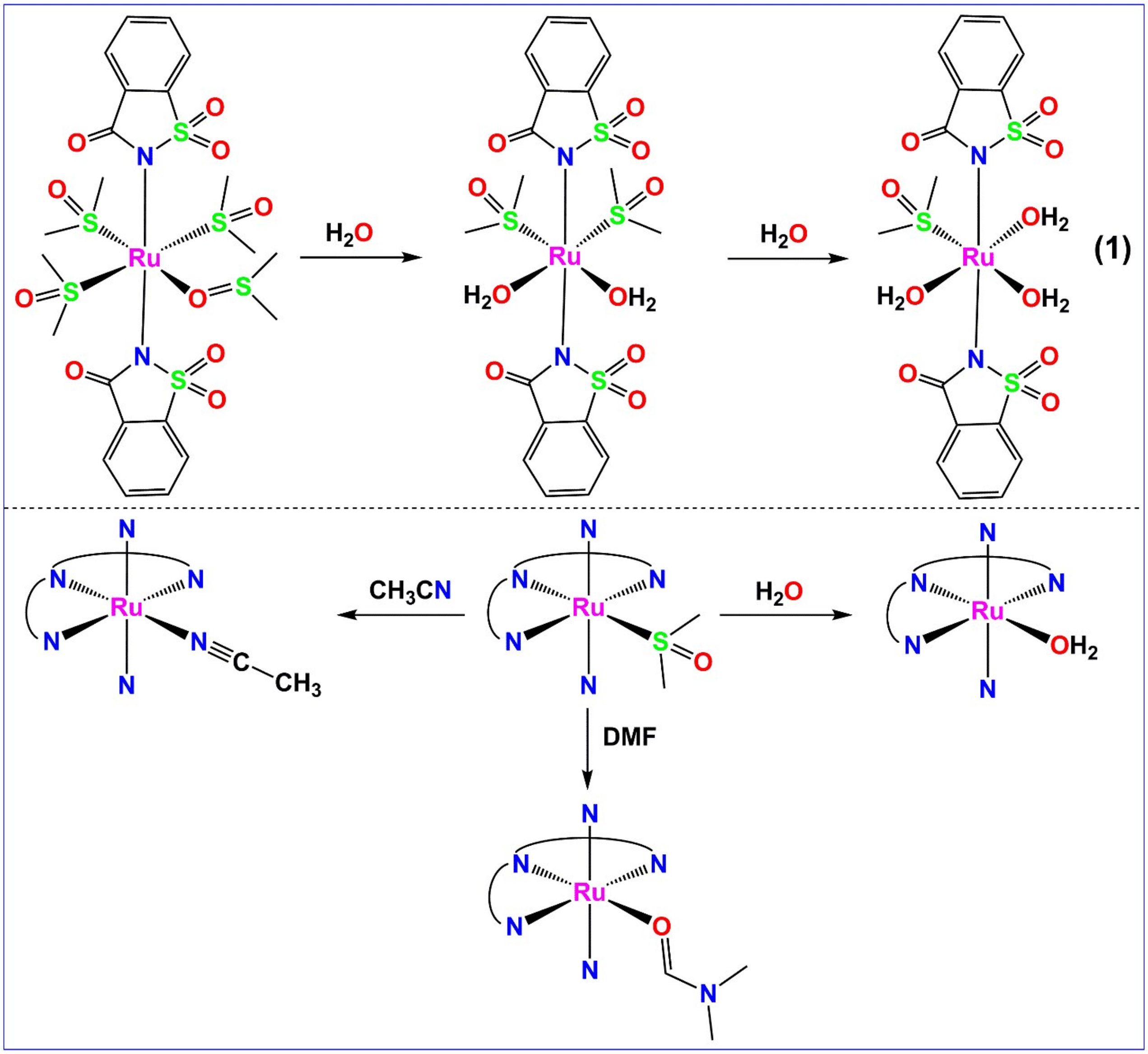

Fig. 5. Proposed solvation reaction of the complexes in various coordinating solvents as identified from their spectral measurements and single-crystal X-ray structures. Solvation of complex **1** in the buffer (top) and generalized representation of complexes [Ru^{II}(R-tpy)(sac)$_2$(X)] (**2-6**) (bottom) in CH_3CN, buffer, and DMF.

concomitant changes in their absorbances. The pseudo first-order kinetic data for the rate of solvation reaction (k) and half-life time ($t_{1/2}$) are measured from the fitting of absorbance changes to the rate equation are shown in Table 3. As expected, the binary complex [Ru(sac)$_2$(H_2O)$_3$(dmso-*S*)] (**1**) showed a higher rate of solvation amongst all complexes with multiple easily accessible labile coordinating ligands. The rates of solvation in DMF were found in order of 10^{-4} s^{-1} and hydrolysis rates in the range of 10^{-4}–10^{-5} s^{-1}. We observed comparatively higher rates of solvation

View Article Online
DOI: 10.1039/D1DT00246E

in the case of DMF than the aqueous buffer, possibly driven by stronger Ru-DMF bonds. The complex **6** seems relatively stable and does not show any noticeable changes in absorbance for 4 h. The solvation and lability of the complexes **1–6** were monitored using time-dependent ^{1}H-NMR in DMSO-d_6 for 3 h (Fig. 4 and Figs. S25–S28). The results showed the ternary speciation of the complexes retained in solution and do not show changes in ligand-centered chemical shifts in aromatic regions. Interestingly, we observed a gradually emerging ^{1}H peak at ~ 2.50 ppm in addition to the residual ^{1}H-peak from the reference solvent (DMSO-d_6) (2.46 ppm), which corresponds to the coordination of solvent (DMSO-d_6) with Ru-center. Upon increasing the time from 10 min to 3 h, the peak at ~ 2.50 ppm showed gradual enhancement in intensity. The time-dependent ^{1}H-NMR data suggests facile solvation and kinetic lability of Ru-X bond, resulting in a dynamic equilibrium between Ru-bound DMSO and free DMSO. The relatively faster solvation for complex **1** and slower solvation for complexes **5** and **6** support the kinetic rates from UV-vis studies (ESI†).

The ligand-exchange reactions with coordinating solvents are evidenced from UV-Vis, ESI-MS, ^{1}H NMR, and the presence of Ru-solvent bond during crystallization from such solvents. Such solvation reactions are shown in Fig. 5. These labile complexes are anticipated to coordinate with biologically relevant molecules as ligands in cancer cells.

Photoreactivity

The photoactivated Ru(II) complexes have been widely explored for PDT/ PACT applications due to activation of a variety of photochemical reactions from easily accessible triplet excited states, facile intersystem crossing, generation of ROS, and presence of intense low-energy absorption bands available in the PDT window [17–22]. The photoexcitation of Ru-polypyridyl complexes having a strong MLCT band in the visible region undergoes photosubstitution of the monodentate ligands by a solvent molecule [55–57]. The presence of a series of R-tpy chromophores in [Ru^{II}(R-tpy)(sac)$_2$(X)] (X = solvent) is anticipated to show photosubstitution of the monodentate saccharin (sac) ligands having therapeutically relevant hypoxia targeting properties due to accessible ^{3}MC-excited states.

The irradiation of white light (WL) (λ_{ex} > 400 nm, 5V, 0.3 W) to the 2% (v/v) DMF-buffer mixture solution (pH 7.2) of complexes **1–6** showed different absorption profiles in comparison to dark (Fig. S29). The complexes **1** and **6** on photo-illumination showed increased absorbance, while **2–5** showed an observable decrease of absorbance. The formation of the isosbestic points in UV-region indicating generation of new photoproducts under visible-light irradiation.

View Article Online
DOI: 10.1039/D1DT00246E

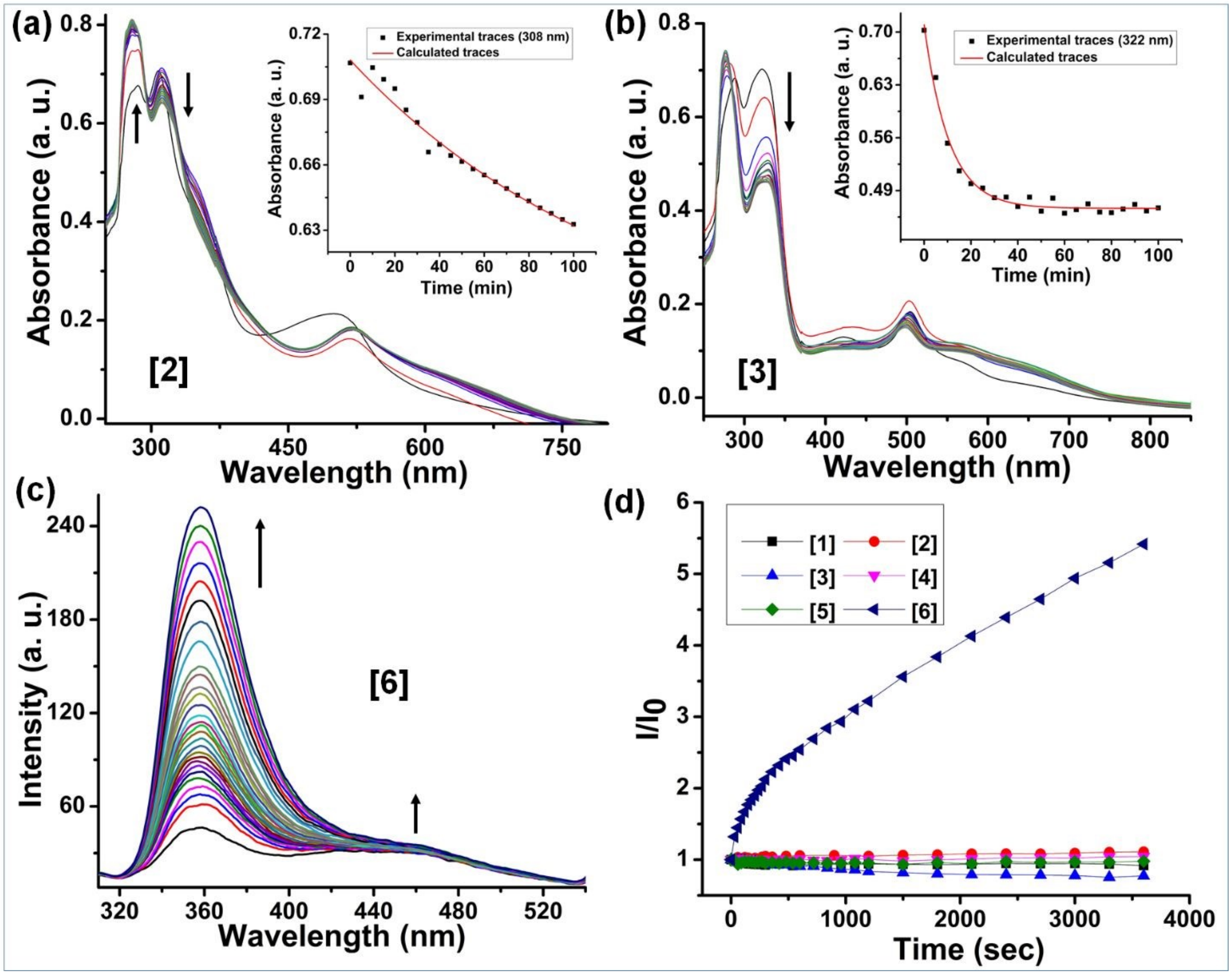

Fig. 6. The green light (λ_{ex} = 530 nm) LED (3V, 158 lm @ 700mA) induced spectral changes observed for the complexes in DMF. (a) Absorption spectral traces of complex **2** (58 μM) for the 0−100 min. Inset: Changes in absorbance at 308 nm of complex **2** with monoexponential curve fitting. (b) Absorption spectral traces of complex **3** (39 μM) for 0−100 min. Inset: Changes in absorbance at 322 nm of complex **3** with monoexponential curve fitting. (c) The unique enhancement of fluorescence emission (λ_{ex} = 280 nm) intensity upon photoexposure of the complex **6** (20 μM) for 0−60 min, (d) Relative changes in the fluorescence intensity of the complexes with the function of exposure time. Ex. slit width = 10 nm, em. slit width = 10 nm, T = 298 K. The direction of the arrow represents the concomitant changes.

We further studied the effect of green LED light (λ_{irr} = 530 nm, 3V, 158 lm @ 700mA, from Luxeonstar LEDs, Canada) on the complexes in DMF from UV-Vis and fluorescence emission studies. The green light (GL) induced significant changes in the UV-vis spectral traces (Figs. 6(a),

View Article Online
DOI: 10.1039/D1DT00246E

(b) and Fig. S30) with alteration in absorbance of both the $\pi \rightarrow \pi^*$ and MLCT bands with the formation of new peaks and formation of multiple isosbestic points.~~.~~

The steady-state emission of complexes **1**−**5** showed a decrease of emission intensity; however, complex **6** displayed a unique emission profile with significant enhancement of emission intensity centered at 359 nm and bands ranging 430−540 nm (Fig. 6(c), (d) and Fig. S31). The emission band at 359 nm corresponds to 3-pytpy, while λ_{em} at 430−540 nm assigned to saccharin. The complexes do not show any changes in their emission intensities in dark (Fig. S32).

Further, GL-induced photoactivity of complex **3** was studied using ^{1}H-NMR spectroscopy. Photoirradiation (0−60 min) resulted in decreased peak intensity at 6.78 ppm and ~ 8.73 ppm with slightly deshielded chemical shifts (Fig. S33). We didn't observe any significant changes in ^{1}H-NMR spectra possibly due to low photosubstitution yield as reported for [Ru^{II}(tpy)LCl$_2$] type complexes, (where L = monodentate ligands: pyridines and nitriles) and higher concentrations (mM) used for NMR studies [58].

The above spectral results suggest distinct green-light induced photoactivity of complexes **2**−**6** due to underlying photo-substitution reactions. The spectral changes occur probably through the photorelease of sac ligands followed by the solvation as reported for several Ru(II)-complexes [27, 28].

DNA binding studies

DNA is the most explored target for many clinically successful chemotherapeutic drugs (e.g. doxorubicins, 5-fluorouracil, gemcitabine, and platins) [59]. Ruthenium complexes with suitable ligands choice can bind DNA in various modes including covalent coordination from electronically rich nucleic acid (Guanine-N7), intercalation in nucleobases, major and minor groove depending on their overall structure [60, 61]. The bound Ru-complexes potentially damage DNA or alter the structural conformations of DNA, leading to inhibition in transcription and translation of cells. The d^6-polypyridyl metal complexes (Ru^{II}/Rh^{III}) have been reported for their advantageous molecular light switch, charge-transfer reagents, metallointercaltors, metalloinsertors of DNA due to their unique luminescence. These properties make these reagents a suitable diagnostic molecular probe and therapeutic agent for cancer [62−65]. The binding of metal complexes to DNA usually shows both hypochromic and bathochromic shifts of their electronic spectra indicating π−π interactions between base pairs and planar organic chromophore.

View Article Online
DOI: 10.1039/D1DT00246E

The addition of CT-DNA to the complexes in 5 mM Tris-HCl/NaCl buffer (pH = 7.2) resulted in a significant decrease in $\pi\rightarrow\pi^*$ and MLCT bands for complexes **2−6** of its UV-Vis spectra corresponding to terpyridine (Figs. 7(a) and S34). However, complex **1** without R-tpy ligand showed a hyperchromic shift of $\pi\rightarrow\pi^*$ band upon DNA addition and can be accounted from duplex stabilization and tight binding with CT-DNA (Fig. S34(a)) [66, 67]. The intrinsic DNA binding constant (K_b) of the complexes found in the order of 10^4 M^{-1}(**1**)−10^6 M^{-1}(**6**) (Table 4). The K_b values are comparable to reported [Ru(Cl-tpy)(en/dach)Cl]Cl complexes (en= ethylenediamine, dach = 1,2-diaminocyclohexane) [67].

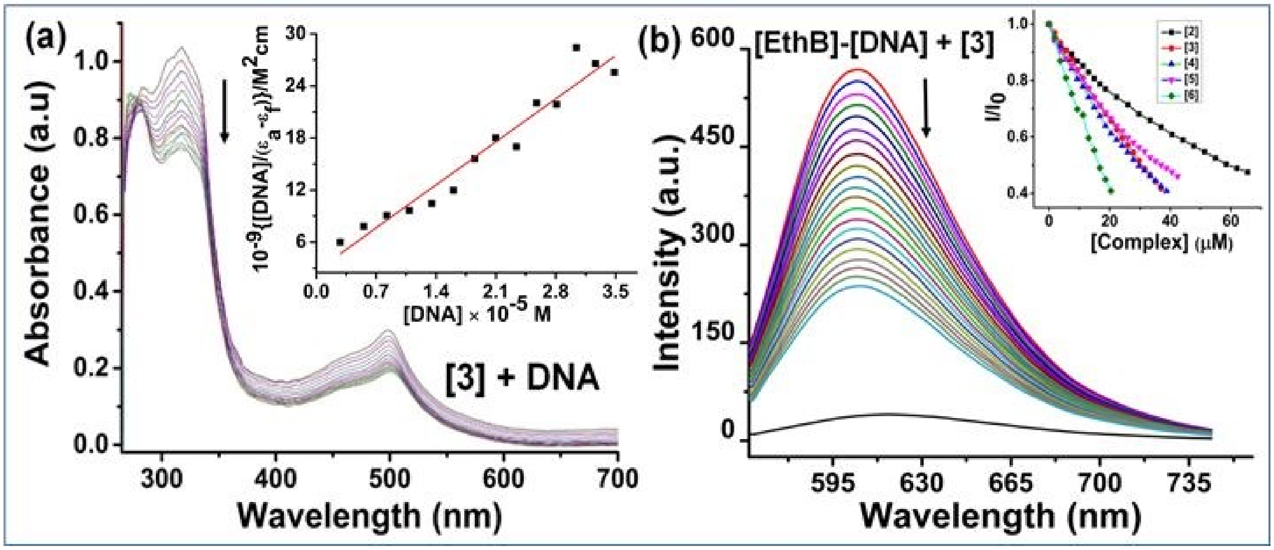

Fig. 7. The interaction of the complexes with CT-DNA in 5 mM Tris-HCl/NaCl buffer (pH = 7.2). (a) The binding of complex **3** (49 μM) with CT-DNA (0−35 μM) in 2.1% (v/v) DMF-buffer mixture leads to the hypochromic shift of their absorption bands. Inset: Determination of binding constant of complex **3** with DNA from the slope to the intercept ratio of the linear fit plot [DNA]/$\Delta\varepsilon_{af}$ vs. [DNA]. (b) Ethidium bromide (EthB) displacement assay for the complex **3.** The gradual addition of complex (0−39 μM) to the multi-step pretreated EthB (12 μM) with CT-DNA (14.4 μM) addition leads to significant quenching of fluorescence intensity of the adduct at 605 nm. The bottom trace (black) corresponds to EthB emission and the top trace (red) corresponds to EthB-DNA adduct. Inset: EthB displacement profile of complexes **2−6** from the quenching of intensity I/I_0 vs [complex] in ~ 2% (v/v) DMF-buffer.

The hypothesis that extended polypyridyls can show intercalation was further studied from ethidium bromide (EthB) displacement assay. EthB is an emissive intercalator for DNA and used as competitive probe for evaluation of intercaltive binding of other compounds. The EtBr alone in

View Article Online
DOI: 10.1039/D1DT00246E

buffer media is poorly emissive due to quenching from H_2O molecule. However, it showed enhanced red emission ~ 605 nm (λ_{exc} = 546 nm) upon binding to DNA [68]. The emissive EthB-DNA adduct upon gradual addition of complexes **2−6** showed a significant fluorescence quenching due to the displacement of EthB from DNA and binding of complexes *via* intercalation (Figs. 7(b) and S35). The competitive apparent binding constant (K_{app}) of complexes are in order of 10^6 derived from their concentration corresponding to 50% emission quenching (C_{50}) (Table 4) [69]. Complex **1** could not quench the emission of EthB-DNA adduct (Fig. S35(a)) signifying the presence of planar R-tpy ligands is necessary for effective intercalation.

Table 4. DNA binding constants for the complexes **1−6**.

Complex	1	2	3	4	5	6
$K_b{}^a$/M^{-1}	1.07×10^5	3.80×10^4	2.65×10^5	3.34×10^4	1.61×10^5	9.50×10^5
$K_{app}{}^b$/M^{-1}	-	5.23×10^6	3.74×10^6	3.97×10^6	3.18×10^6	7.00×10^6
$^cC_{50}$ (μM)	-	58.47	31.50	29.67	36.95	16.80

^{a}Intrinsic DNA binding constant. ^{b}Apparent binding constant with DNA. ^{c}The complex concentration corresponding to 50% quenching of emission intensity of EthB-DNA adduct.

Protein binding studies

Serum proteins play an active role in the binding, distribution, metabolism, and pharmacokinetics of drugs. The clinically tested anticancer Ruthenium complexes (NAMI-A and KP1019) show less toxicity and tumor selectivity and are believed to act through HSA-mediated transport.

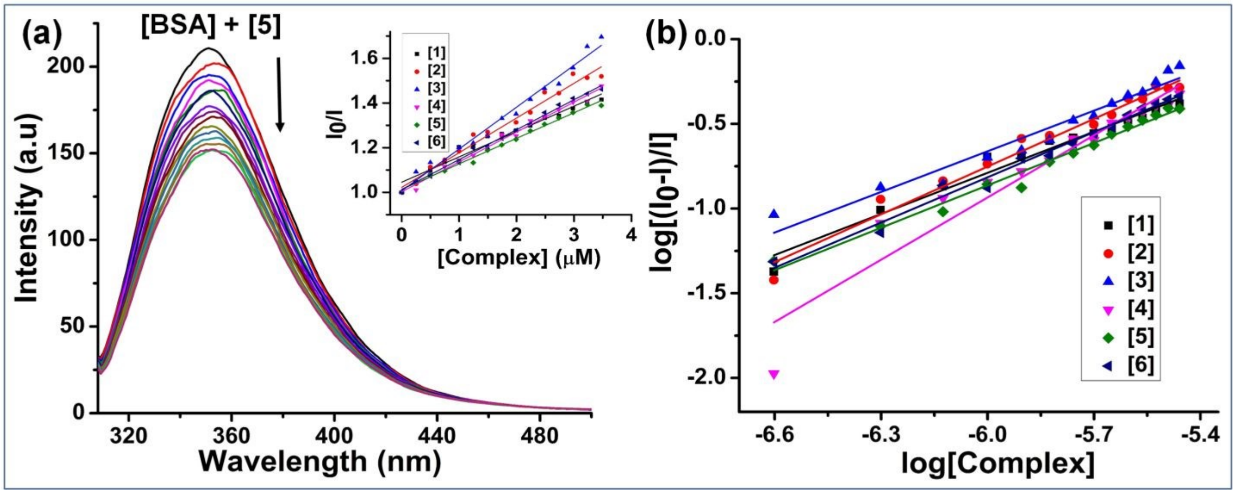

View Article Online
DOI: 10.1039/D1DT00246E

Fig. 8. The BSA (2 μM) binding studies of the complexes (0−3.5 μM) in 0.7% (v/v) DMF−5 mM Tris-HCl/NaCl buffer (pH = 7.2) mixture at 298 K, $\lambda_{exc/em}$ = 295/345 nm and slit width ex/em = 10/5. (a) The tryptophan fluorescence emission quenching of BSA upon increasing complex **5.** Inset: The Stern-Volmer plot for the complexes. (b) The modified Stern-Volmer plot for the determination of static equilibrium binding constant from intercept and number of binding sites available (*n*) from the slope of the plot.

Table 5. BSA binding parameters for the complexes **1**−**6**.

Complex	1	2	3	4	5	6
$K_{BSA}{}^{a}$ (M^{-1}) × 10^{5}	1.14	1.55	1.87	1.34	1.14	1.34
$K_{q}{}^{b}$ (M^{-1}s^{-1}) × 10^{13}	1.14	1.55	1.87	1.34	1.14	1.34
K^{c} (M^{-1}) × 10^{4}	1.16	7.62	1.36	258	1.38	3.33
n^{d}	0.81	0.94	0.80	1.22	0.83	0.89

[a]Stern-Volmer constant for tryptophan-214 fluorescence emission quenching of BSA. [b]Quenching rate constant. [c]Protein binding constant. [d]The number of binding sites per molecule of BSA.

These Ru-compounds binds to the most abundant serum protein accumulate in tumor cells via leaky blood vessels by the enhanced permeability retention (EPR) effect [70, 71]. The presence of two tryptophan residues (Trp-134 and Trp-212) contributes to its significant intrinsic fluorescence in BSA and is used as a spectral probe for drug binding studies. The alteration of fluorescence arises from the conformational changes, ligand binding, subunit association, or protein denaturation [72, 73].

A significant quenching of fluorescence intensity of BSA (2 μM) at 346 nm (λ_{exc} = 295 nm) was observed upon the gradual addition of complexes **1**−**6** (0−3.5 μM) (Fig. 8 and Fig. S36). The Stern-Volmer quenching constant (K_{BSA}), Stern-Volmer quenching rate constant (K_q), the binding constant (K), and the number of binding sites available per molecule (n) were determined [74] and shown in Table 5. The binding constants vary in the range 10^4−10^6 M^{-1}, suggesting an optimum affinity towards BSA with lowest affinity for complex **1** and highest for complex **4**. The n values are closer to unity (0.80−1.22), suggesting a single binding site available per molecule of the protein. The protein binding parameters K_{BSA}, K_q, K, and n values agree with the reported Ru-terpyridine ternary complexes [75].

Synchronous fluorescence spectral studies

View Article Online
DOI: 10.1039/D1DT00246E

Lloyd introduced that the simultaneous scanning of both the excitation and emission monochromators and monitoring fluorescence provides a valuable synchronous fluorescence spectrum (SFS) [76]. The constant-wavelength or constant-energy or variable-angle synchronous luminescence measurement can serve various analytical needs. The SFS provides several valuable information such as spectral simplifications, reduced spectral bandwidth, and maintained fluorescence sensitivity of multichromophoric residues with different spectral properties [77]. The information on drug interactions with protein is crucially essential in the proteomics era, and the SFS technique provides salient information at the molecular level.

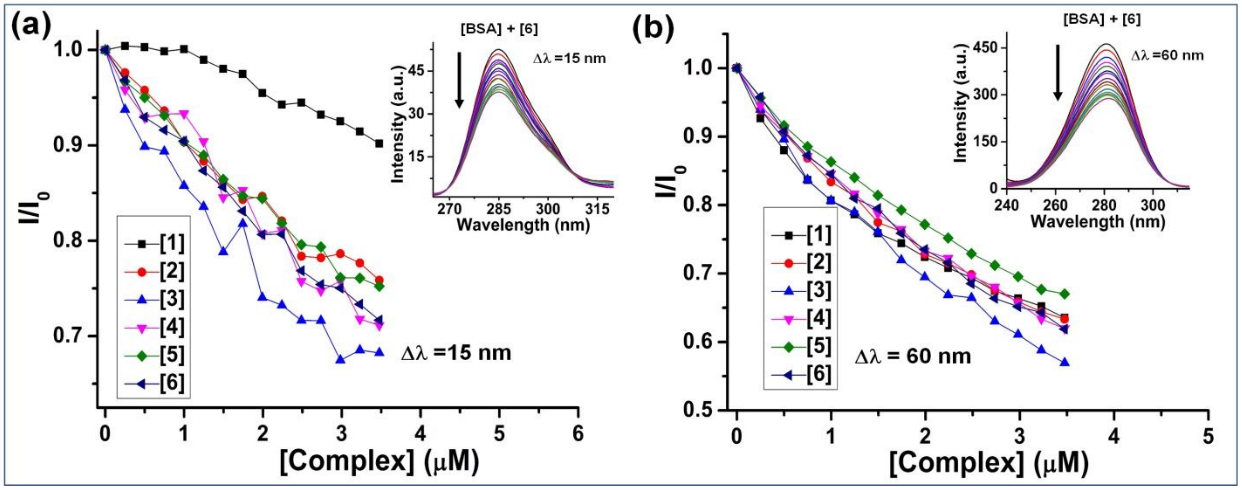

Fig. 9. The synchronous fluorescence binding studies of BSA (2 μM) of the complexes **1−6** in 0.7% (v/v) 5 mM Tris-HCl/NaCl buffer (pH = 7.2) mixture at 298 K slit width ex/em = 10/5. (a) An overlay of I/I_0 vs. [Complex] for the decrease of intensity for $\Delta\lambda$ = 15 nm. Inset: The spectral traces showing an intensity decrease of complex **6**. (b) An overlay of I/I_0 vs. [Complex] for the decrease of intensity for $\Delta\lambda$ = 60 nm. Inset: The spectral traces show an intensity decrease of complex **6**.

The fixed wavelength scanning of BSA with $\Delta\lambda$ = 15 nm and $\Delta\lambda$ = 60 nm exploits the information of tryptophan and tyrosine chromophores present in the microenvironment of the protein. The addition of aliquots of the complexes **1−6** to buffer solution of BSA (2 μM) resulted in significant quenching of intensity for both the $\Delta\lambda$ = 15 nm (10−32%) and $\Delta\lambda$ = 60 nm (33−44%) measurements (Fig. 9 and Figs. S37−S38). The pronounced changes in the intensity for $\Delta\lambda$ = 60 nm suggests the preferential binding with tryptophan residue over tyrosine. However, we did not observe many changes in the hydrophobicity of the microenvironment around tryptophan residue with no apparent shift of band position at $\Delta\lambda$ = 60 nm [78].

View Article Online
DOI: 10.1039/D1DT00246E

Photoinduced singlet oxygen generation

The ability of the complexes to induce singlet oxygen ($^1O_2$) generation upon photoexposure of green light LED (GL, λ_{irr} = 530 nm) (3V, 158 lm @ 700mA) was performed from the absorption spectral measurement of 1,3-diphenylisobenzofuran (DPBF). DPBF in the presence of $^1O_2$ undergoes [4+ 2] cycloaddition reaction resulting in the formation of highly unstable endoperoxide, which subsequently decomposes to 1, 2-dibenzoylbenzene (DBB) [79, 80]. We performed DPBF assay to investigate $^1O_2$ generation from complexes **2** and **4** upon GL exposure, and results are shown in Fig. 10 and Fig. S39. Interestingly, the DPBF (50 μM) remains stable in the presence of the complexes (10 μM) in dark. However, GL illumination (0–600 s) showed a remarkable decrease in $A_{415\text{ nm}}$ corresponding to π–π* electronic transition of DPBF. The control experiment with DPBF alone upon GL exposure only showed a slight decline of $A_{415\text{ nm}}$, suggesting the photoinduced *in situ* generations of $^1O_2$ from the complexes **2** and **4.** The significant decrease of $A_{415\text{ nm}}$ for complex **4** (96%) than **2** (54%) indicates efficient $^1O_2$ generation from the thienyl substituent of R-tpy. The presence of three thienyl moieties in imidazophenantroline ligand design in TLD1443- a Ru-based PDT agent under clinical trial for bladder cancer is critical for higher $^1O_2$ quantum yield [24].

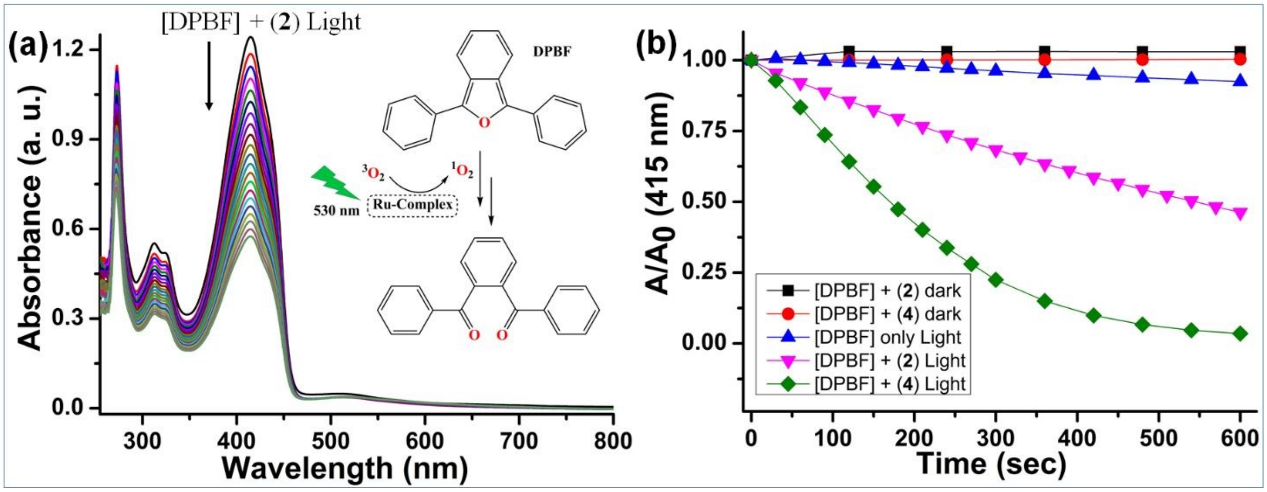

Fig. 10. (a) Absorption spectral profile of DPBF (50 μM) with **2** (10 μM) upon irradiation with green light LED (λ =530 nm) for 0–600 s signifying the formation of $^1O_2$. (b) Time-dependent relative absorbance changes for complexes **2** (10 μM) and **4** (10 μM) with DPBF (50 μM) in dark and upon green light irradiation. Spectra was recorded at 298 K in DMF solution.

Cytotoxicity Studies

Photocytotoxicity

View Article Online
DOI: 10.1039/D1DT00246E

The cytotoxicity profile of the selected complexes (**1**, **2**, and **4**) were tested in both the HeLa and MCF7 cancer cells in the dark and low energy UV-A light (365 nm, 6 W) irradiation using MTT assay (Fig. 11 and Figs. S40, S42 in ESI). The tested complexes showed relatively higher toxicity towards HeLa over MCF7 cells in the dark. Complex **4** with 2-thienyl-tpy group found more cytotoxic than the binary Ru(II) compound (**1**) and ternary complex **2** having 2-pyrrolyl-tpy ligand.

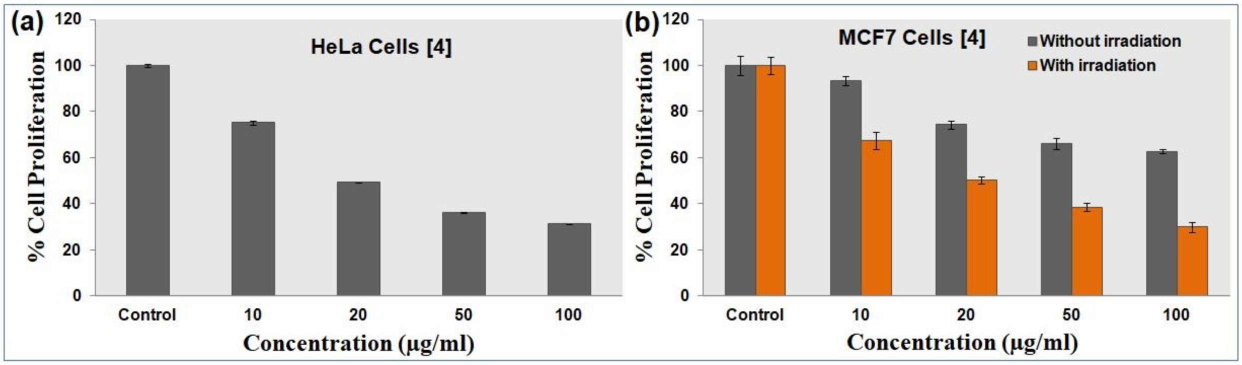

Fig. 11. The dose-dependent toxicity profile of complex **4** from the MTT assay was determined after 24 h incubation. (a) Cytotoxicity profile in the dark for HeLa cells. (b) The overlay of dark toxicity and UV-A light (365 nm, 6 W) induced phototoxicity in MCF7 cells.

Further, the photocytotoxicity of the complexes in MCF7 cells were also studied in the presence of white light ($\lambda_{ex} > 400$ nm, 5V, 0.3 W) (Fig. S41). We observed enhanced phototoxicity of complex **4** in MCF7 cells at 365 nm UV-A light compared to white light irradiation. In contrast, complexes **1** and **2** do not differ in their phototoxicities to the MCF7 cells in UV-A light. This greater phototoxicity for complex **4** can be accounted from its efficient ROS generation due to presence of 2-thienyl substituted terpyridine (ttpy) as observed from DPBF assay compared to complex **2**. The presence of labile Ru-solvent bonds and associated ligand-exchange reactions are also expected to deactivate the triplet Ru-excited states essential to generate $^1O_2$ or other ROS involved in photocytotoxicity.

Cellular uptake in MCF7 and HeLa cancer cells

Once the cytotoxicity of the complexes was studied, we attempted to study their uptake to both the HeLa and MCF7 cell lines from the fluorescence microscopic imaging studies. As the complexes are fluorescent and showed blue emission, the compounds' uptake can be visualized using confocal laser scanning microscopy (CLSM).

View Article Online
DOI: 10.1039/D1DT00246E

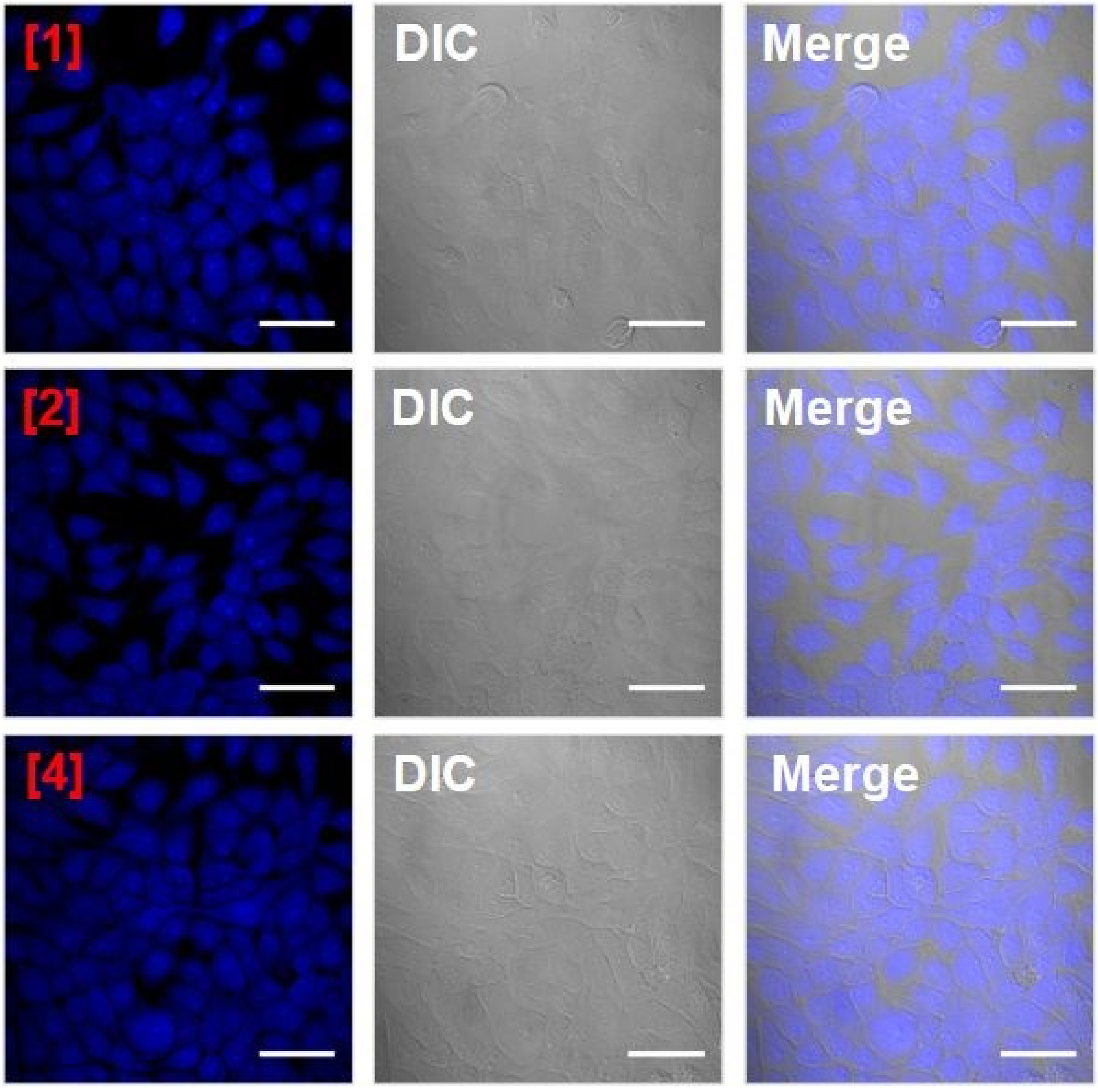

Fig. 12. Cellular uptake of complexes **1**, **2** and **4** (10 μM) in MCF7 cells after 4 h of treatment visualized by confocal laser scanning microscopy with λ_{ex} = 350 nm and λ_{em} = 460 nm. Top: complex **1**, middle: complex **2** and bottom: complex **4**, scale bar = 50 μm.

The cellular uptake studies of complexes in MCF7 cells are shown in Fig. 12 and for HeLa cells in Fig. S43 in ESI. Both the cells showed efficient localization of the complexes throughout the cytoplasm and nucleus. Good permeability of the complexes to the cancer cells is advantageous in targeting aggressive and hypoxic tumors.

Photoinduced intracellular ROS detection

To convince ourselves on the photocytotoxicity mechanism, we studied the intracellular ROS generation in the presence of the tested Ru(II) complexes. 2',7'-dichlorodihydrofluorescein diacetate

View Article Online
DOI: 10.1039/D1DT00246E

(H_2DCFDA), a cell-permeable probe, which upon cleavage of the acetate groups by esterases and oxidation is converted to highly fluorescent 2',7'-dichlorofluorescein (DCF) and utilized as an indicator for ROS detection [81]. To affirm the role of the photosensitizing complexes **1**, **2**, **4** as reactive oxygen species (ROS) generating agents, we performed DCFH-DA staining in MCF7 cells. The control experiments were performed in the dark as negative control and hydrogen peroxide (H_2O_2) as a conventional positive control. After 4 h treatment of complexes and photoirradiation (1 h) of low energy UV-A light (365 nm, 6 W), we observed significant ROS generation capability of the complexes. Complex **4** showed higher ROS generation ability than **1** and **2** (Fig. 13). The efficient ROS generation ability from complex **4** was consistent with the results obtained from photodegradation of 1,3-diphenylisobenzofuran (DPBF) (Fig. 10) and higher phototoxicity in MCF7 cells (Fig. 11). In the dark control experiment, very feeble ROS was detected in the presence the complexes (Fig. S44). The positive control H_2O_2 elicit significant ROS generation (Fig. 13 (a), 2nd panel). The results are quantitated by mean fluorescence intensity (MFI) analysis using Image J software suggesting higher efficiency of complex **4** (Fig. 13(b)).

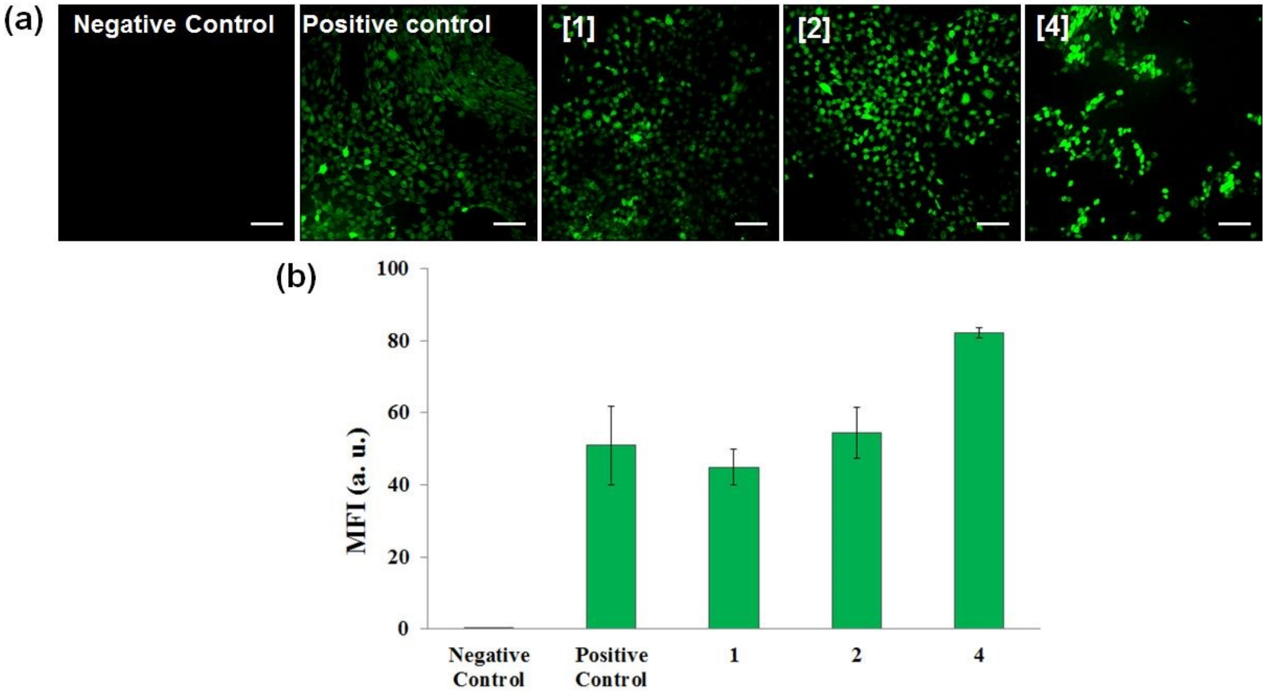

Fig. 13. Detection of intracellular reactive oxygen species (ROS) from H_2DCFDA assay. (a) The confocal laser scanning microscopy (CLSM) images of MCF7 cells, for untreated cells (negative control), H_2O_2

View Article Online
DOI: 10.1039/D1DT00246E

treated (positive control) and after 4 h treatment with complexes **1**, **2**, **4** (10 µM) followed by photoexposure (1 h) with UV-A light (365 nm). λ_{ex} = 492 nm, λ_{em} = 527 nm, scale bar = 100 µm. (b) Quantitative analysis comparing the levels of ROS intermediates in untreated and treated MCF7 cells on exposure to UV-A light (365 nm). Values are mean ± S.D from three independent experiments (n = 3).

Apoptosis assessment

The apoptotic potential of complexes **1**, **2,** and **4** was substantiated on MCF7 cells in the dark (Fig. 14). The viable cells, early apoptotic cells, and the late apoptotic cells were examined by acridine orange/ethidium bromide (AO/EB) dual staining which efficiently binds to nucleic acids by intercalation [82]. These fluorescent dyes exactly aid in distinguishing cells in definite stages of apoptosis. Acridine orange (AO), a vital dye, stains both the viable (green colour) and apoptotic cells (yellow-green). Ethidium bromide (EtBr) stains necrotic cells red due to loss of membrane integrity. Early apoptotic cells show characteristic features of nuclear condensation and apoptotic bodies in yellow color. Late apoptotic cells are marked orange-red as they incorporate EtBr demonstrating aberrant nuclear morphology. The confocal laser scanning microscopy images of AO/EB staining indicate that complex **4** showed enhanced apoptosis compared to complexes **1** and **2**. Most of the cells appeared orange-red in color, representative of late apoptosis. Quantification of apoptosis affirms complex **4** causes efficient apoptosis as compared to **1** and **2** (Fig. 14 (b)).

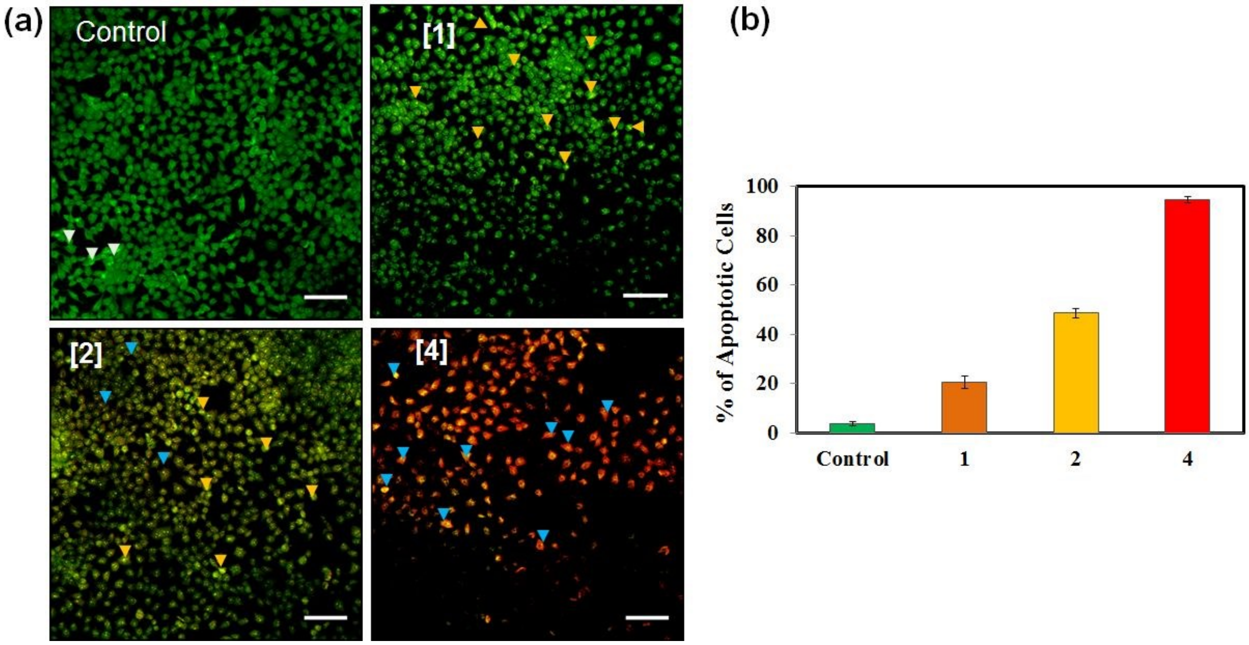

View Article Online
DOI: 10.1039/D1DT00246E

Fig. 14. Detection of apoptosis by acridine orange (AO) and ethidium bromide (EtBr) dual staining in MCF7 cell lines. (a) The confocal laser scanning microscopy (CLSM) images (20X) after incubation of 24 h with the complexes **1**, **2**, **4** (10 μM) for 24 h. Untreated cells stained in green homogenously demonstrate normal morphology (white arrow), early apoptosis is observed in yellow as chromatin condensation (yellow arrow) and late apoptosis is observed as yellow/orange colour with characteristic nuclear fragmentation and blebbing (blue arrow). Scale bar = 100 µm. (b) Quantification of viable and apoptotic cells treated with complexes **1**, **2**, **4** (n = 3).

Conclusion

In this work, a series of six Ru(II) complexes containing 4′-substituted terpyridines (R-tpy) as a DNA intercalator and photosensitizer and bioactive saccharin as a carbonic anhydrase-IX (CA-IX) inhibitor were synthesized, and their physicochemical and spectroscopic properties were evaluated. All the ternary [Ru^{II}(R-tpy)(sac)$_2$(solv)] complexes containing a solvent-coordinated site (Ru-solv) to impart kinetic lability and bioreactivity. The solid-state structures from X-ray diffraction studies for complexes **1**, **3**, **4**, and **5** displayed {RuN$_5$(solvent)} distorted octahedral geometries from N$_3$-donor R-tpy and two *trans*-N-donor saccharinate (sac) ligands. The labile complexes undergo solvation reactions in DMF, and aqueous buffer evidenced by UV-vis and ^{1}H-NMR kinetic studies. We also observed the electronic effects of ancillary R-tpy ligands over the Ru-X bond lability. They exhibit moderate binding interactions with duplex DNA and BSA under physiological conditions. The synchronous fluorescence studies qualitatively indicate preferential binding of the complexes in the tryptophan microenvironment of BSA. The photoactivity of the complexes upon irradiation with the lower-energy green LED light at 530 nm showed characteristic absorption and emission spectral changes corresponding to the possible dissociation and release of saccharin. The tested complexes remain cytotoxic in dark for HeLa and MCF7 cells. Complexes induce the formation of reactive oxygen species (ROS) upon photoirradiation of low energy UV-A light (365 nm) supporting the PDT effect. The intracellular generation of ROS was detected using DCFDA as ROS-sensitive dye. Interestingly, complex **4** showed enhanced photo-cytotoxicity in MCF7 cells, which could be accounted for from efficient PACT or PDT effect originating from 4′-(2-thienyl) terpyridine (ttpy) ligand. The confocalimaging studies demonstrate sufficient permeability, accumulation of the emissive Ru(II) complexes inside the cancer cells. The dual acridine organe/ethidium bromide staining suggests effective induction of apoptosis, especially for complex **4**. The complexes could

View Article Online
DOI: 10.1039/D1DT00246E

be suitable for selective targeting the hypoxic and aggressive tumor cells *via* affecting the photo-release of saccharin as a CA-IX inhibitor.

Experimental Section

Materials, Methods, and Instrumentations

2-pyridine carboxaldehyde and 3-pyridine carboxaldehyde were purchased from Avra Synthesis Pvt. Ltd. (Hyderabad) and used with no further purification. Furfural, 2-thiophene carboxaldehyde, and pyrrole-2-carboxaldehyde were purchased from Sigma Aldrich. $RuCl_3.xH_2O$ was purchased from Arora Matthey Pvt. Ltd. India sodium saccharinate (98%) from SDFCL, 1,3-diphenylisobenzofuran (DPBF) from Alfa Aesar, India. All these chemicals were used as received. Calf thymus (CT) DNA and ethidium bromide (EThB) were procured from Sigma chemicals (U. S. A.) and bovine serum albumin (BSA, fraction V) was procured from SRL, India. 2′,7′-Dichlorofluorescin diacetate (DCFH-DA), Acridine orange (AO), Ethidium bromide (EtBr) were procured from Sigma Aldrich.

Solvents were obtained from commercial sources and were used after purification as described in the literature [83]. The 4′- substituted-2,2′:6,2″-terpyridines (R-tpy) were prepared by the following literature procedure [84]. Trypsin- ethylenediaminetetraacetic acid (trypsin-EDTA), Dulbecco’s modified eagle’s medium (DMEM) and 3-(4,5-dimethylthiazol-2-yl)-2,5-diphenyltetrazolium bromide (MTT) were all procured from Sigma-Aldrich. Penicillin-streptomycin antibiotic solution (100X) was procured from Himedia. Dimethyl sulfoxide (DMSO), formaldehyde was obtained from Merck Chemicals, India. Fetal bovine serum (FBS) was purchased from Gibco Life Technologies. Human cervical carcinoma (HeLa) cells were obtained from National Centre for Cell Science (NCCS), Pune. Human breast carcinoma (MCF-7) cells were procured as a kind gift from Prof. Bushra Ateeq, Indian Institute of Technology Kanpur, India. Tris-(hydroxymethyl)-aminomethane-HCl-NaCl (Tris-HCl/NaCl) buffer was prepared using Milli-Q water of specific resistance of 18.2 MΩ. The *cis*-$[Ru(dmso\text{-}S)_3(dmso\text{-}O)Cl_2]$, a metal precursor was synthesized as reported in the literature [85].

Mass spectral measurement was done using a water Q-TOF electrospray ionization mass spectrometer (ESI-MS). Infrared (IR) spectra were carried out on a Perkin-Elmer model 1300 FT-IR spectrometer in KBr pellets in 4000−400 cm^{-1} range. NMR spectra recorded on JEOL 400 MHz and 500 MHz spectrometers in DMSO-d6 and referenced to deuterated solvent (secondary reference) and chemical shifts measured relative to tetramethylsilane (TMS). Fluorescence spectra were recorded on an Agilent Cary Eclipse fluorescence spectrometer at 298 K and UV-vis absorption spectra were obtained using a Varian V670 and Perkin-Elmer Lambda 25 spectrometers. Cyclic voltammetric measurements were performed in DMF using a CH Instrument Model CHI 610E potentiostat containing platinum wire as the auxiliary electrode, Ag/AgCl as a reference electrode, and glassy carbon as a working electrode. Tetrabutylammonium perchlorate (TBAP) solution was used as a supporting electrolyte.

Synthesis of the complexes

Trans-[Ru(sac)$_2$(H$_2$O)$_3$(dmso-*S*)] (**1**)To the warm methanolic solution of *cis*-[Ru(dmso-*S*)$_3$(dmso-*O*)Cl$_2$] (200 mg, 0.41 mmol) was added with a methanolic solution of sodium saccharinates (200 mg, 0.82 mmol) and refluxed for the next 4 h where a greenish solution was obtained. The solution was dried in a vacuum and crystallized in methanol−water as a green solid. The suitable crystal was chosen for single-crystal x-ray diffraction studies. The product was filtered and washed with 3 × Et$_2$O to get complex **1** as a greenish solid.

Yield: 354 mg (60%). ESI-MS (H$_2$O): *m/z* 680.92 [Ru(sac)$_2$(dmso)$_2$(H$_2$O)$_2$+Na$^+$]$^+$ (calc. for $C_{18}H_{24}N_2NaO_{10}S_4Ru$: *m/z* 680.93), *m/z* 644.91 [Ru(sac)$_2$(dmso)$_2$+Na$^+$]$^+$ (calc. for $C_{18}H_{20}N_2NaO_8S_4Ru$: *m/z* 644.90). FT-IR (KBr, *n*/cm^{-1}): 3534 (w), 3376 (w), 3103 (w), 3013 (w), 2931 (w), 1643 (vs, sh), 1587 (m), 1459 (w), 1405 (w), 1334 (w), 1292 (m), 1258 (vs, sh), 1148 (vs, sh), 1117 (s), 1099 (s), 1051 (m), 1015 (s), 971 (s), 951 (m), 930 (m), 774 (w), 747 (m, sh), 721 (w), 706 (w) 676 (s, sh), 633 (w), 610 (m), 544 (m), 530 (m), 426 (w) [vs, very strong; s, strong; m, medium; w, weak; br, broad; sh, sharp]. ^{1}H NMR (400 MHz, DMSO-*d*$_6$) δ 7.63 (m, *J* = 12.4, 5.6, 2.9 Hz, 8H), 2.54 (s, 9H). UV-Visible in DMF [λ_{max}, nm (e, M^{-1} cm^{-1})]: 275 (2640) and 365 (368). UV-Visible in 5 mM Tris-HCl/NaCl buffer (pH = 7.2)-DMF mixture (100: 1) [λ_{max}, nm (e, M^{-1} cm^{-1})]: 270 (2120) and 344 (256).

Synthesis of complexes 2−6.

The complexes **2−6** was synthesized from following a general synthetic route (Scheme 2) in which methanol solution of complex **1** (100 mg, 0.17 mmol) added with CHCl$_3$ solution of 4′- substituted-2,2′:6′,2″-terpyridines (R-tpy, 0.17 mmol) where, X = 2-pyrolyl (ptpy) (**2**), 2-furyl (ftpy) (**3**), 2-thienyl (ttpy) (**4**), 2-pyridyl (2-pytpy) (**5**) and 3-pyridyl (3-pytpy) (**6**) and refluxed overnight to obtained dark brownish red solution.

[Ru(ptpy)(sac)$_2$(dmso)] (**2**)

View Article Online
DOI: 10.1039/D1DT00246E

Yield: 120 mg (80%). ESI-MS (CH_3CN): *m/z* 623.04 [M-(sac)-(dmso)+(CH_3CN)]$^+$ (calc. for $C_{28}H_{21}N_6O_3SRu$: *m/z* 623.04). FT-IR (KBr *ν*/cm^{-1}): 3428 (m, br), 3065 (w), 3013 (w), 2923 (w), 1972 (w), 1642 (s), 1586 (m) 1458 (m) 1434 (w), 1334 (w), 1290 (m), 1257 (s, sh), 1148 (vs, sh), 1118 (m), 1099 (m), 1051 (m), 1015 (m), 970 (m), 951 (m), 880 (w), 786 (w), 772 (w), 754 (m), 747 (m), 725 (w), 705 (w), 676 (m), 633 (w), 605 (w), 595 (w), 543 (w), 529 (w), 425 (w). ^{1}H NMR (500 MHz, DMSO-*d*$_6$) δ 9.65 – 8.60 (m, 4H), 8.33 – 7.16 (m, 17H), 6.38 (d, *J* = 39.3 Hz, 1H). UV-Visible in DMF [λ_{max}, nm (ε, M^{-1} cm^{-1})]: 288 (18330), 310 (17770), 350 (11860) and 515 (5020). UV-Visible in 5 mM Tris-HCl/NaCl buffer (pH = 7.2)-DMF mixture (100: 1) [λ_{max}, nm (ε, M^{-1} cm^{-1})]: 286 (15840) and 459 (4820).

[Ru(ftpy)(sac)$_2$(dmso)] (3)

Yield: 124 mg (83%). Single-crystals was obtained from slow evaporation of complex CH_3CN-MeOH (1:1) solution. ESI-MS (MeOH): *m/z* 661.02 [M-(sac)]$^+$ (calc. for $C_{18}H_{23}N_4O_5S_2Ru$: *m/z* 661.02) FT-IR (KBr *ν*/cm^{-1}): 3430 (s, br), 2929 (w), 1731 (w), 1619 (vs, sh), 1582 (s), 1480 (w), 1458 (w), 1432 (w), 1338 (w), 1288 (s), 1253 (s), 1149 (vs, sh), 1119 (m), 1097 (m), 1053 (m), 1015 (m), 951 (m), 884 (w), 788 (m), 754 (m), 679 (m), 633 (w), 595 (m), 559 (w), 542 (w), 524 (w). ^{1}H NMR (500 MHz, DMSO-*d*$_6$) δ 9.69 – 8.52 (m, 5H), 8.43 – 7.15 (m, 15H), 7.02 – 6.72 (m, 1H). UV-Visible in DMF [λ_{max}, nm (ε, M^{-1} cm^{-1})]: 322 (24670), and 505 (6730). UV-Visible in 5 mM Tris-HCl/NaCl buffer (pH = 7.2)-DMF mixture (100: 1) [λ_{max}, nm (ε, M^{-1} cm^{-1})]: 322 (22590) and 500 (6550).

[Ru(ttpy)(sac)$_2$(dmso)] (4)

Yield: 128 mg (84%). Single-crystals was obtained from slow diffusion of *n*-hexane in complex MeOH-CH_2Cl_2 (1:1) solution. ESI-MS (CH_3CN): *m/z* 676.99 [M-(sac)]$^+$ (calc. for $C_{28}H_{23}N_4O_4S_3Ru$: *m/z* 676.99). FT-IR (KBr *ν*/cm^{-1}): 3419 (m, br), 3068 (m, br), 1630 (s), 1587 (m), 1478 (w), 1461 (m), 1429 (m), 1396 (w), 1344 (m) 1296 (vs, sh), 1256 (s), 1170 (vs), 1157 (vs), 1124 (m), 1058 (w), 1014 (w), 952 (w), 882 (w), 859 (w), 839 (w), 786 (s), 753 (m), 729 (w), 706 (w), 678 (m), 653 (w), 596 (s, sh), 554 (s), 541 (w), 520 (w), 481 (w). ^{1}H NMR (500 MHz, DMSO-*d*$_6$) δ 9.39 (s, 1H), 9.21 (q, *J* = 10.5, 9.0 Hz, 2H), 9.00 (d, *J* = 25.6 Hz, 2H), 8.81 – 8.19 (m, 3H), 8.08 – 7.95 (m, 2H), 7.82 (s, 1H), 7.66 – 7.43 (m, 8H), 7.41 – 7.33 (m, 1H), 7.27 (t, *J* = 6.3 Hz, 1H). UV-Visible in DMF [λ_{max}, nm (ε, M^{-1} cm^{-1})]: 288 (20530), 322 (24600) and 504 (7590). UV-Visible in 5 mM Tris-HCl/NaCl buffer (pH = 7.2)-DMF mixture (100: 1) [λ_{max}, nm (ε, M^{-1} cm^{-1})]: 285 (22380), 321 (23040), 333 (23840) and 497 (6840).

View Article Online
DOI: 10.1039/D1DT00246E

[Ru(2-pytpy)(sac)$_2$(dmso)] (5)

Yield: 130 mg (86%). Single-crystal was obtained from diffusion of diethyl ether in MeOH-CH_2Cl_2 mixture (1:1). ESI-MS (MeOH): *m/z* 777.02 [M-(dmso)+H$^+$]$^+$ (calc. for $C_{34}H_{23}N_6O_6S_2Ru$: *m/z* 777.02), *m/z* 672.03 [M-(sac)]$^+$ (calc. for $C_{29}H_{24}N_5O_4S_2Ru$: *m/z* 672.03). FT-IR (KBr ν/cm^{-1}): 3435 (s, br), 2923 (m), 1627 (s), 1582 (s), 1459 (m), 1416 (m), 1331 (m), 1252 (s), 1145 (vs, sh), 1119 (s), 1052 (m), 1018 (m) 951 (m), 781 (m), 754 (m), 679 (m), 632 (w), 595 (m), 542 (w), 523 (w). ^{1}H NMR (400 MHz, DMSO-d_6) δ 9.64 (s, 1H), 9.28 – 9.16 (m, 1H), 8.84 (dd, J = 105.3, 8.1 Hz, 4H), 8.15 (m, 3H), 7.84 – 7.44 (m, 12H), 7.29 – 7.23 (m, 1H). UV-Visible in DMF [λ_{max}, nm (ε, M^{-1} cm^{-1})]: 288 (25180), 316 (21390) and 496 (7790). UV-Visible in 5 mM Tris-HCl/NaCl buffer (pH = 7.2)-DMF mixture (100: 1) [λ_{max}, nm (ε, M^{-1} cm^{-1})]: 285 (26490), 331 (16140) and 489 (7100).

[Ru(3-pytpy)(sac)$_2$(dmso)] (6)

Yield: 122 mg (80%). ESI-MS (MeOH): *m/z* 672.03 [M-(sac)]$^+$ (calc. for $C_{29}H_{24}N_5O_4S_2Ru$: *m/z* 672.03). FT-IR (KBr ν/cm^{-1}): 3430 (m), 3065 (w), 2920 (w), 1975 (w), 1636 (s), 1582 (m), 1458 (w), 1437 (w), 1400 (w), 1331 (w), 1286 (s), 1254 (s), 1148 (vs, sh), 1119 (s), 1053 (m), 1018 (m), 952 (m), 790 (m), 755 (m), 734 (w), 705 (w), 680 (m), 632 (w), 605 (m), 596 (m), 555 (w), 544 (w), 525 (w), 425 (w). ^{1}H NMR (500 MHz, DMSO-d_6) δ 10.54 – 7.07 (m, 22H). UV-Visible in DMF [λ_{max}, nm (ε, M^{-1} cm^{-1})]: 284 (29560), 320 (20250), 497 (6890) and 560 (3320). UV-Visible in 5 mM Tris-HCl/NaCl buffer (pH = 7.2)-DMF mixture (100: 1) [λ_{max}, nm (ε, M^{-1} cm^{-1})]: 279 (25290), 317 (16090) and 491 (5140).

X-ray structure determination

The single crystals of complexes **1, 3, 4,** and **5** were obtained at ambient conditions, and similar efforts for complexes **2** and **6** were unsuccessful. Single crystal of suitable quality was mounted at 100(2) K on a Bruker Aplex-II CCD with Mo-Kα source of X-ray radiation (λ = 0.71073 Å). Data collection was performed by multiscan ω-scan technique and further processed and reduction from SAINT (Bruker) [86]. The SADABS [87] program was used for absorption correction and an integrated program SHELXT for space group and structure determination [88]. Structure refinement was processed from SHELXL [89] and Olex2 software packages [90] by full-matrix least square technique for F^2. All hydrogen atoms were added with suitable hybridizations and refined with a riding model. The disordered structure of complexes was fixed from DFIX, ISOR, and EADP for bond length, isotopic approximations, and ADP respectively. We were unable to model the disordered solvent model, therefore, solvent mask from Olex2 was applied, which may account for

View Article Online
DOI: 10.1039/D1DT00246E

CH_3CN (**3**), *n*-hexane (**4**) and diethyl ether (**5**) as solvent of crystallization and were consistent with the number of electrons per unit cell [82]. The CCDC numbers of the complexes are 2057838 (**1**), 2057839 (**3**), 2057840 (**4**), and 2057841 (**5**). The ORTEP-III [91] was used for structure display. The details of crystallographic refinement parameters are shown in table 2 and selected bond lengths and bond angles are shown in table S3−S4.

Solubility and stability of the complexes

All the complexes were soluble in MeOH, EtOH, $CHCl_3$, CH_2Cl_2, DMF, and DMSO. Only complex **1** showed solubility in H_2O. The complexes were insoluble in n-pentane, *n*-hexane, diethyl ether, tetrahydrofuran, ethyl acetate, toluene, and benzene. The complexes were fairly stable in solid-state and undergo solvation in the presence of potential coordinating solvents. The rate of salvation was studied from time-dependent UV-visible measurement, and rate constants (K) and half-life ($T_{1/2}$) were determined from monoexponential first-order kinetics by following equations (1) and equations (2)

$A = C_0 + C_1 e^{-KT}$ ……………………(1)

$T_{1/2} = 0.693/K$ ……………………(2)

where, time = T at absorbance = A, and C_0 and C_1 are constants obtained upon fitting.

Photoactivity of the complexes

The complex DMF solution of a known concentration was photoexposed with the green light (λ_{exc} = 530 nm, 3V, 158 lm @ 700mA) from Luxeon Star LEDs of SP-01 series, SinkPAD-II™ Rebel Star LED assembly and white light (λ_{ex} > 400 nm, 5V, 0.3 W) fixed at the cuvette top. The UV-Vis and fluorescence spectra of the solution were recorded at regular intervals separately. Both the exposure experiments were performed in a dark room to avoid interference of external light in the measurement. Further, the dark scanning of the spectral measurement was also performed to identify the photoirradiation effects of the samples.

DNA binding, Ethidium bromide displacement assay, and Protein binding experiments

DNA binding was measured from absorption spectral titration of the complex solution with CT-DNA and the intrinsic binding equilibrium constant (K_b) was determined from changes in the corresponding decrease in absorbance with the gradual addition of CT-DNA. The ethidium bromide displacement (EthB) was performed from fluorescence titration of highly fluorescent EthB-DNA adduct with the gradual addition of complexes with a known binding affinity of EthB of with DNA ($K_{EthB} = 1 \times 10^7$). The binding affinity of complexes with BSA was evaluated from fluorescence

View Article Online
DOI: 10.1039/D1DT00246E

titration of complexes to the emissive protein at ~345 nm (λ_{exc} = 295 nm) and Stern-Volmer quenching constant (K_{BSA}), quenching rate constants (K_q), the static equilibrium binding constant (K) and the number of binding sites (n) per molecule of BSA was determined from intensity plot. The synchronous fluorescence titration of the complex with BSA determined with wavelengths $\Delta\lambda$ = 15 nm and $\Delta\lambda$ = 60 nm to study the preferences of the complexes towards tyrosine and tryptophan residue binding. All the binding studies are described in our recent publications in detail [92, 93].

Photoinduced singlet oxygen generation

Singlet oxygen generation ($^1O_2$) from the complexes (10 μM) upon green light (λ_{exc} = 530 nm) LED (3V, 158 lm @ 700mA) irradiation was detected by photooxidation of 1,3-diphenylisobenzofuran (DPBF) to 1,2-dibenzoylbenzene (DBB) using absorption measurement in DMF. The decrease of absorbance at $A_{415\ nm}$ for DPBF (50 μM) in presence complexes as a function of exposure time corresponds to $^1O_2$ generation and DBB formation [94]. The control experiments of complexes with DPBF in dark and only DPBF upon light illumination were performed under similar conditions.

Cellular studies

Cell viability (MTT) assay

The quantification of cytotoxicity of complexes was determined from colorimetric assay *i.e.* MTT (3-(4,5-dimethylthiazol-2-yl)-2,5-diphenyltetrazoliumbromide) recorded by UV/Vis microplate reader (Multiskan Spectrum, Thermo Scientific) at 570 nm [95]. HeLa and MCF-7 cell lines were cultured in Dulbecco's minimum essential medium (DMEM) supplemented with 10% FBS (Invitrogen, USA), penicillin (100 U/ml), and streptomycin (100 ug/ml) at 37 °C and 5% CO_2 in a humidified incubator. The culture medium in tissue culture flasks was changed every alternate day and confluent flasks were trypsinized with trypsin-ethylenediaminetetraacetic acid (trypsin-EDTA) followed by cell seeding. Almost 5 $\times 10^3$ cells were cultured into 96 well plates for 7 hours to get the desired morphology of the cells. The cells were further treated in a dose-dependent manner with varying concentrations of the synthesized complexes for 24 h. After 24 h, the media was discarded and the cells were incubated with MTT reagent (200 μL, 0.5 mg/ml in serum-free DMEM) for 4 h in a 5% CO_2 humidified incubator at 37 °C. Further, the MTT reagent was removed, and 200 μL DMSO was added to solubilize the purple formazan crystals formed. The reduction of tetrazolium ring of yellow-colored MTT (3-(4,5-dimethylthiazol-2-yl)-2,5-diphenyltetrazolium bromide) to purple formazan crystals allows for quantification of cell viability (%). Considering the 100% viability of the controls (untreated) cells, the data was recorded at 570 nm, which is proportional to

View Article Online
DOI: 10.1039/D1DT00246E

the number of metabolically active cells ($n = 3$). Absorbance was measured using a microtiter plate reader Multiskan UV-Vis spectrophotometer.

Photocytotoxicity assay

The cytotoxic potential of complexes upon light irradiation was quantitated by photocytotoxicity assay in the MCF-7 cell line. The protocol adapted is similar to the previous MTT assay procedure with 5×10^3 cells treated with an increasing concentration of compounds only for 4 hours to avoid any false-positive results. Herein, cells were divided into two groups *i.e.* (i) the dark controls pertain to assays involving the differential gradient of compounds but, not exposed to light and (ii) cells irradiated with low energy white light (WL, $\lambda_{ex} > 400$ nm) and UV-A light of 365 nm (6W) for 1 h. After exposure of MCF-7 cells for 4 h with compounds, cells were incubated with fresh DMEM to avoid any effect of the uninternalized samples and photo-irradiated for 1h. The control samples were also maintained in dark for a similar duration. The samples were incubated at 37 ^{0}C in a humidified incubator for a total time duration of 24 hours after photo-irradiation. MTT reagent (200 μL, 0.5 mg/ml in serum-free DMEM) was added to each well and incubated at 37 °C in a 5% CO_2 humidified incubator for 4 hours. Further, the MTT reagent was removed, and 200 μL DMSO was added to solubilize the purple formazan crystals formed. Absorbance indicating cell viability was measured at 570 nm by Multiscan UV- Vis spectrophotometer (n = 3).

Cellular uptake studies

The cellular localization of complexes **1, 2, 4** were examined using a confocal laser scanning microscope (CLSM) in MCF-7 and HeLa cell lines. Both the cells (5×10^4 cells) were incubated with complexes **1**, **2,** and **4** (10 μM) for 4 hours at 37°C in a 5% CO_2 humidified incubator in 24 well plates containing 0.2% gelatin-coated glass coverslips. The media was removed after incubation of cells with complexes **1**, **2,** and **4** followed by washing with 1X PBS thrice. Cells were further fixed with a 4% formaldehyde solution for 20 min and washed again 1X PBS thrice to ensure complete removal of fixative. The washed coverslips with a monolayer of cells were mounted on a glass slide with a buffered mounting medium (to avoid fading and drying) and observed under CLSM at appropriate wavelengths. The images procured were processed using ZEN blue, Adobe Photoshop CS5, and ImageJ.

Measurement of intracellular reactive oxygen species (ROS)

Intracellular ROS levels in the MCF7 cell line were detected by 2′,7′ -dichlorofluorescein diacetate (DCFH-DA) staining [96]. Briefly, MCF7 cells (5×10^4 cells per well) were cultured in 24 well

View Article Online
DOI: 10.1039/D1DT00246E

tissue culture plates coated with 0.2% gelatin. Cells were treated with complexes (10 µM) at 37^0C for 4 h to evaluate ROS generation. Herein, the cells were divided into two groups *i.e.* (i) the dark controls pertain to assays not exposed to light and (ii) cells irradiated with UV-A light of 365 nm (6 W) for 1 h. After exposure with compounds for 4 h, cells were replaced with fresh DMEM to circumvent any effect of the uninternalized samples and photo-irradiated for 1h. The control samples were also maintained in dark for a similar duration. The samples were incubated at 37^0C in a humidified incubator for a total time duration of 24 hours after photo-irradiation. Cells were treated with hydrogen peroxide (200 µM), a conventional ROS inducer for 45 minutes aiding as a positive control. The cells were washed with PBS after incubation time and stained with DCFH-DA (10 µm) for 30 minutes. Further, ROS was measured by CLSM imaging under appropriate lasers. ROS generation was also quantitated by mean fluorescence intensity (MFI) values (n = 10) for each set using Image J software.

Acridine orange / Ethidium bromide dual fluorescent staining for cell apoptosis

Cell apoptotic efficiency of complexes was analyzed by Acridine orange/Ethidium bromide (AO/EtBr) staining in MCF7 cell line [97]. Briefly, MCF7 cells (5×10^4 cells per well) were cultured in 24 well tissue culture plates and incubated with complexes (10 µM) for 24 hours at 37^0C and 5% CO_2 humidified condition. After incubation, the cells were washed with phosphate buffer saline (PBS) and stained with AO (100 µg/mL in PBS) and EtBr (100 µg/mL in PBS) at room temperature for 20 minutes. The stained MCF7 cells were visualized by CLSM (20X magnification) under suitable laser channels. Cell apoptosis (%) was quantified as the number of apoptotic cells divided by the total number of cells (n = 3).

Acknowledgment

The authors gratefully thank the Indian Council of Medical Research (ICMR) (Project no. 2020-2677) and the Science and Engineering Research Board (SERB) (Project no. EMR/2016/000521) for financial support. P. Kumar thanks the University Grant Commission (U. G. C.) for the research fellowship.

References

1. E. A. Seddon and K. R. Seddon, *The Chemistry of Ruthenium*, Elsevier Science Publication BV, Amsterdam, 1984.
2. T. Naota, H. Takaya and S.-I. Murahashi, *Chem. Rev.*, 1998, **98**, 2599−2660.

DOI: 10.1039/D1DT00246E

3. C. S. Allardayce and P. J. Dyson, *Platinum Met. Rev.*, 2001, **45**, 62−69.
4. J. Reedijk, *Platinum Met. Rev.*, 2008, **52**, 2−11.
5. S. Campagna, F. Puntoriero, F. Nastasi, G. Bergamini and V. Balzani, *Photochemistry and Photophysics of Coordination Compounds: Ruthenium*, eds. V. Balzani and S. Campagna, Springer, Berlin, Heidelberg, 2007, vol. 280, pp. 117–214.
6. K. Kalyanasundaram, *Coord. Chem. Rev.*, 1982, **46**, 159−244.
7. J. J Soldevila-Barreda and P. J Sadler, *Curr. Opin. Chem. Biol.,* 2015, **25**, 172−185.
8. A. R. Simovic´, R. Masnikosa, I. Bratsos, E. Alessio, *Coord. Chem. Rev.*, 2019, **398**, 113011.
9. W. H. Ang and P. J. Dyson, *Eur. J. Inorg. Chem.,* **2006**, 4003–4018.
10. X. Li, A. K. Gorle, M. K. Sundaraneedi, F. R. Keene and J. G. Collins, *Coord. Chem. Rev.*, 2018, **375**, 134–147.
11. M. Jakubaszek, B. Goud, S. Ferrari and G Gasser, *Chem. Commun.,* 2018, **54**, 13040–13059.
12. M. J. Chow, C. Licona, G. Pastorin, G. Mellitzer, W. H. Ang and C. Gaiddon, *Chem. Sci.*, 2016, **7**, 4117–4124.
13. M. J. Chow, M. Alfiean, G. Pastorin, C. Gaiddon and W. H. Ang, *Chem. Sci.*, 2017, **8**, 3641–3649.
14. L. Zeng, P. Gupta, Y. Chen, E. Wang, L. Ji, H. Chao and Z.-S. Chen, *Chem. Soc. Rev.,* 2017, **46**, 5771–5804.
15. S. Thota, D. A. Rodrigues, D. C. Crans and E. J. Barreiro, *J. Med. Chem.*, 2018, **61**, 5805–5821.
16. R. G. Kenny and C. J. Marmion, *Chem. Rev.*, 2019, **119**, 1058−1137.
17. N. J. Farrer, L. Salassa and P. J. Sadler, *Dalton Trans.*, 2009, 10690–10701.
18. C. Mari, V. Pierroz, S. Ferrari and G. Gasser, *Chem. Sci.*, 2015, **6**, 2660–2686.
19. A. P. Castano, T. N. Demidova and M. R. Hamblin, *Photodiagn. Photodyn. Ther.* 2004, **1,** 279–293.
20. I. J. Macdonald and T. J. Dougherty, *J. Porphyrins Phthalocyanines,* 2001, **5**, 105–129.
21. L. M. Lifshits, J. A. Roque III, P. Konda, S. Monro, H. D. Cole, D. von Dohlen, S. Kim, G. Deep, R. P. Thummel, C. G. Cameron, S. Gujar, and S. A. McFarland, *Chem. Sci.*, 2020, **11**, 11740–11762.
22. F. E. Poynton, S. A. Bright, S. Blasco, D. C. Williams, J. M. Kelly and T. Gunnlaugsson, *Chem. Soc. Rev.,* 2017, **46**, 7706–7756.

DOI: 10.1039/D1DT00246E

23. D. A. Smithen, H. Yin, M. H. R. Beh, M. Hetu, T. S. Cameron, S. A. McFarland and A. Thompson, *Inorg. Chem.*, 2017, **56**, 4121−4132.
24. S. Monro, K. L. Colon, H. Yin, J. Roque, P. Konda, S. Gujar, R. P. Thummel, L. Lilge, C. G. Cameron and S. A. McFarland, *Chem. Rev.*, 2019, **119**, 797–828.
25. J. D. Knoll, B. A. Albani and C. Turro, *Acc. Chem. Res.,* 2015, **48**, 2280−2287.
26. J. D. Knoll and C. Turro, *Coord. Chem. Rev.*, 2015, **282−283**, 110−126.
27. T. N. Rohrabaugh, Jr, A. M. Rohrabaugh, J. J. Kodanko, J. K. White and C. Turro, *Chem. Commun.,* 2018, **54**, 5193−5196.
28. S. Bonnet, *Dalton Trans.*, 2018, **47**, 10330–10343.
29. B. S. Howerton, D. K. Heidary and E. C. Glazer, *J. Am. Chem. Soc.,* 2012, **134**, 8324–8327.
30. L. N. Lameijer, D. Ernst, S. L. Hopkins, M. S. Meijer, S. H. C. Askes, S. E. L. Dévédec and S. Bonnet, *Angew. Chem.*, 2017, **129**, 11707 –11711.
31. J. Zhao, W. Li, S. Gou, S. Li, S. Lin, Q. Wei and G. Xu, *Inorg. Chem.*, 2018, **57**, 8396–8403.
32. L. Zeng, Y. Chen, H. Huang, J. Wang, D. Zhao, L. Ji and H. Chao, *Chem. Eur. J.*, 2015, **21**, 15308–15319.
33. A. Sharma, J. F. Arambula, S. Koo, R. Kumar, H. Singh, J. L. Sessler and J. S. Kim, *Chem. Soc. Rev.*, 2019, **48**, 771−813.
34. M. G. V. Heiden, L. C. Cantley, C. B. Thompson, *Science*, 2009, **324**,1029–1033.
35. B. P. Mahon, C. O. Okoh and R. McKenna, *Future Oncol.*, 2015, **11**, 2117− 2119.
36. B. P. Mahon, A. M. Hendon, J. M. Driscoll, G. M. Rankin, S. A. Poulsen, C. T. Supuran and R. McKenna, *Bioorg. Med. Chem.*, 2015, **23**, 849–854.
37. K. Köhler, A. Hillebrecht, J. Schulze Wischeler, A. Innocenti, A. Heine, C. T. Supuran and G. Klebe, *Angew. Chem., Int. Ed.*, 2007, **46**, 7697–7699.
38. *(a)* M. Rami, J.-Y. Winum, A. Innocenti, J.-L. Montero, A. Scozzafava and C. T. Supuran, *Bioorg. Med. Chem. Lett.*, 2008, **18**, 836–841; *(b)* C. T. Supuran, F. Mincione, A. Scozzafava, F. Briganti, G. Mincione and M. A. Ilies*, Eur. J. Med. Chem.*, 1998, **33**, 247−254.
39. P. Kumar, S. Dasari, A. K. Patra, *Eur. J. Med. Chem.*, 2017, **136**, 52−62.
40. C. Icsel, V. T. Yilmaz, S. Aydinlik and M. Aygun, *Dalton Trans.,* 2020, **49**, 7842–7851.
41. C. Icsel and V. T. Yilmaz, *J. Photochem. Photobiol. B,* 2014, **130**, 115−121.

View Article Online
DOI: 10.1039/D1DT00246E

42. J. P. Sauvage, J. P. Collin, J. C. Chambron, S. Guillerez, C. Coudret, V. Balzani, F. Barigelletti, L. De Cola and L. Flamigni, *Chem. Rev.*, 1994, **94**, 993–1019.
43. S. Campagna, F. Puntoriero, F. Nastasi, G. Bergamini, V. Balzani, V. Balzani and S. Campagna (Ed.), *Photochemistry and Photophysics of Coordination Compounds I*, Springer Berlin Heidelberg, Berlin, Heidelberg, 2007, pp. 117–214.
44. M. Beley, D. Delabouglise, G. Houppy, J. Husson and J.-P. Petit, *Inorg. Chim. Acta,* 2005, **358**, 3075−3083.
45. B. S. Paraj´on-Costa and E. J. Baran, *Monatsh. Chem*., 1995, **126**, 673−679.
46. W. Goodall, K. Wild, K. J. Arm and J. A. G. Williams, *J. Chem. Soc., Perkin Trans.,* 2002, **2**, 1669–1681.
47. E. A. Medlycott and G. S. Hanan, *Chem. Soc. Rev.*, 2005, **34**, 133–142.
48. L. M. Loftus, K. F. Al-Afyouni, T. N. Rohrabaugh Jr., J. C. Gallucci, C. E. Moore, J. J. Rack and C. Turro, *J. Phys. Chem. C*, 2019, **123**, 10291–10299.
49. M. H. Al-Afyouni, T. N. Rohrabaugh Jr., K. F. Al-Afyouni and C. Turro, *Chem. Sci.*, 2018, **9**, 6711–6720.
50. V. H. S. van Rixel, B. Siewert, S. L. Hopkins, S. H. C. Askes, A. Busemann, M. A. Siegler and S. Bonnet, *Chem. Sci.,* 2016, **7**, 4922–4929
51. J. Kargesa, O. Blacque, M. Jakubaszek, B. Goud, P. Goldner, G. Gasser, *J. Inorg. Biochem*., 2019, **198**, 110752.
52. R. -A. Fallahpour, M. Neuburger and M. Zehnder, *Polyhedron*, 1999, **18**, 2445−2454.
53. J. Reedijk, *Platinum Met. Rev*., 2008, **52**, 2–11.
54. F. Wang, A. Habtemariam, E. P. L. van der Geer, R. Fernández, M. Melchart, R. J. Deeth, R. Aird, S. Guichard, F. P. A. Fabbiani, P. Lozano-Casal, I. D. H. Oswald, D. I. Jodrell, S. Parsons and P. J. Sadler, *P. Natl. Acad. Sci. U. S. A.,* 2005, **102**, 18269−18274.
55. S. Bonnet, J.-P. Collin, *Chem. Soc. Rev.*, 2008, **37**, 1207 –1217.
56. C. R. Hecker, P. E. Fanwick, D. R. McMillin, *Inorg. Chem.*, 1991, **30**, 659 – 666.
57. A. -C. Laemmel, J. -P. Collin, J. -P. Sauvage, *Eur. J. Inorg. Chem.,* 1999, 383 – 386.
58. H.-F. Suen, S. W. Wilson, M. Pomerantz, and J. L. Walsh, *Inorg. Chem.,*1989, **28**, 786–791.
59. A. Ali and S. Bhattacharya, *Bioorgan. Med. Chem.*, 2014, **22**, 4506−4521.
60. B. J. Pages, D. L. Ang, E. P. Wright and J. R. Aldrich-Wright, *Dalton Trans.*, 2015, **44**, 3505–3526.

View Article Online
DOI: 10.1039/D1DT00246E

61. V. Brabec and J. Kasparkova, *Coord. Chem. Rev.*, 2018, **376**, 75−94.
62. J. C. Genereux and J.K. Barton, *Chem. Rev.*, 2010, **110**, 1642−1662.
63. M. R. Gill and J.A. Thomas, *Chem. Soc. Rev.*, 2012, **41**, 3179−3192.
64. J. M. Kelly, A. B. Tossi, D. J. McConnell and C. OhUigin, *Nucleic Acids Res.*, 1985, **13** 6017−6034.
65. B. M. Zeglis, V. C. Pierre and J. K. Barton, *Chem. Commun.,* 2007, 4565−4579.
66. F. Dimiza, A. N. Papadopoulos, V. Tangoulis, V. Psycharis, C. P. Raptopoulou, D. P. Kessissoglou, G. Psomas, *J. Inorg. Biochem.*, 2012, **107**, 54–64.
67. D. Lazić, A. Arsenijević, R. Puchta, Ž. D. Bugarčić and A. Rilak, *Dalton Trans.*, 2016, **45**, 4633–4646.
68. M. J. Waring, *J. Mol. Biol.*, 1965, **13**, 269−282.
69. M. Lee, A. L. Rhodes, M. D. Wyatt, S. Forrow and J. C. Hartley, *Biochemistry*, 1993, **32**, 4237−4245.
70. A. Bijelic, S. Theiner, B. K. Keppler and A. Rompel, *J. Med. Chem.,* 2016**, *59***, 5894−5903.
71. M. Liu, Z. J. Lim, Y. Y. Gwee, A. Levina and P. A. Lay, *Angew. Chem. Int. Ed.,* 2010**, 49**, 1661−1664.
72. M. R. Eftink and C. A. Ghiron, *J. Phys.Chem.,* 1976, **80**, 486−493.
73. D. S. Raja, G. Paramaguru, N. S. P. Bhuvanesh, J. H. Reibenspies, R. Renganathan and K. Natarajan, *Dalton Trans.* 2011, **40**, 4548−4559.
74. G. Rabbani, E. J. Lee, K. Ahmad, M. H. Baig and I. Choi, *Mol. Pharmaceut.* 2018**, 15**, 1445−1456.
75. M. M. Milutinović, A. Rilak, I. Bratsos, O. Klisurić, M. Vranes, N. Gligorijević, S. Radulović and Ž. D. Bugarčić, *J. Inorg. Biochem.*, 2017, **169**, 1–12
76. J. B. F. Lloyd, *Nat. Phys. Sci.*, 1971, **231**, 64−65.
77. S. Das, A. M. Powe, G. A. Baker, B. Valle, B. El-Zahab, H. O. Sintim, M. Lowry, S. O. Fakayode, M. E. McCarroll, G. Patonay, M. Li, R. M. Strongin, M. L. Geng, and I. M. Warner, *Anal. Chem.*, 2012, **84**, 597−625.
78. N. Ibrahim, H. Ibrahim, S. Kim, J. -P. Nallet and F. Nepveu, *Biomacromolecules*, 2010, **11**, 3341–3351.
79. Y. Sun, L. E. Joyce, N. M. Dickson and C. Turro, *Chem. Commun.*, 2010, **46**, 2426–2428.

View Article Online
DOI: 10.1039/D1DT00246E

80. V. D. Singh, R. S. Singh, B. K. Dwivedi, S. Mukhopadhyay, A. Shukla, P. Maiti, and D. S. Pandey, *J. Phys. Chem. C*, 2019, **123**, 30623–30632.
81. *(a)* D. Wu and P. Yotnda, *J. Visualized Exp.*, 2011, **57**, e3357; *(b)* J. Wei and A. K. Renfrew, *J. Inorg. Biochem.*, 2018, **179**, 146–153.
82. D. Baskić, S. Popović, P. Ristić and N. N. Arsenijević, *Cell Biol. Int. Rep.*, 2006, **30**, 924–932.
83. D. D. Perrin, W. L. F. Armarego and D.R. Perrin, Purification of Laboratory Chemicals, Pergamon, Oxford, 1980.
84. A. Maroń, A. Szlapa, T. Klemens, S. Kula, B. Machura, S. Krompiec, J. G. Małecki, A. Świtlicka-Olszewska, K. Erfurt and Anna Chrobok, *Org. Biomol. Chem.*, 2016, **14**, 3793−3708.
85. I. P. Evans, A. Spencer and G. Wlkinson, *J. Chem. Soc. Dalton Trans*., 1973, 204−209.
86. N. Walker and D. Stuart, *Acta Crystallogr. Sect. A*, 1983, **39,** 158–166.
87. G. M. Sheldrick, SADABS, *Area Detector Absorption Correction*, University of Göttingen, Göttingen, Germany, 2001.
88. G. M. Sheldrick, *Acta Cryst.*, 2015, A**71**, 3−8.
89. G. M. Sheldrick, *Acta Cryst.*, 2015, **C71**, 3−8.
90. O. V. Dolomanov, L. J. Bourhis, R. J. Gildea, J. A. K. Howard and H. Puschmann, *J. Appl. Crystallogr.*, 2009, **42**, 339–341.
91. M. N. Burnett and C. K. Johnson, *ORTEP-III, Report ORNLe 6895*, Oak Ridge National Laboratory, Oak Ridge, TN, 1996.
92. P. Kumar, S. Swagatika, S. Dasari, R. S. Tomar and A. K. Patra; *J. Inorg. Biochem*., 2019, **199**, 110769.
93. P. Kumar, R. J. Butcher and A. K. Patra; *Inorg. Chim. Acta,* 2020, **506**, 119532.
94. T. Entradas, S. Waldron and M. Volk, *J. Photochem. Photobiol. B*, 2020, **204**, 111787.
95. T. Mossman, *J. Immunol. Methods*, 1983, **65**, 55−63.
96. A. K. Maparu, P. Singh, B. Rai, A. Sharma, S. Sivakumar, *Mater. Sci. Eng. C*, 2021, **119**, 111577.
97. P. Elumalai, D. N. Gunadharini, K. Senthilkumar, S. Banudevi, R. Arunkumar, C. S. Benson, G. Sharmila and J. Arunakaran, *Toxicol. Lett.*, 2012, **215**, 131–142.